Review

Magnetar QPOs and Neutron Star Crust Elasticity

[Hajime Sotani](#) [*]

Review

Magnetar QPOs and Neutron Star Crust Elasticity

Hajime Sotani [1,2,3] (ID)

[1]   Astrophysical Big Bang Laboratory, RIKEN, Saitama 351-0198, Japan
[2]   Interdisciplinary Theoretical & Mathematical Science Program (iTHEMS), RIKEN, Saitama 351-0198, Japan
[3]   Theoretical Astrophysics, IAAT, University of Tübingen, 72076 Tübingen, Germany
[*]   Correspondence: sotani@yukawa.kyoto-u.ac.jp

Abstract: The crust region is a tiny fraction of neutron stars, but it has a variety of physical properties and plays an important role in astronomical observations. One of the properties characterizing the crust is the elasticity. In this review, with the approach of asteroseismology, we systematically examine neutron star oscillations excited by crust elasticity, adopting the Cowling approximation. In particular, by identifying the quasi-periodic oscillations observed in magnetar flares with the torsional oscillations, we make a constraint on the nuclear saturation parameters. In addition, we also discuss how the shear and interface modes depend on the neutron star properties. Once one detects an additional signal associated with neutron star oscillations, one can get a more severe constraint on the saturation parameters and/or neutron star properties, which must be a qualitatively different constraint obtained from terrestrial experiments, and help us to complementarily understand astrophysics and nuclear physics.

Keywords: neutron stars; equation of state; asteroseismology

---

1. Introduction

Neutron stars produced through the core-collapse supernova at the last moment of the massive star's life can become in extreme states, which is quite difficult to realize on Earth. For example, their density easily exceeds the standard nuclear density, $\sim 0.16 \text{ fm}^{-3}$, and the gravitational and magnetic fields around/inside the star become much stronger than those observed in our solar system [1]. Therefore, physics in such extreme states may be revealed through the observations of neutron stars and/or their phenomena.

The stellar structure depends on the equation of state (EOS) for neutron star matter, which is under beta-equilibrium and charge neutrality. However, the determination of EOS for neutron star matter from the experiments is still difficult. This is because the density of nuclei is around the saturation density almost independently of nuclear species, due to the nature of nuclear saturation properties. Nevertheless, the saturation parameters characterizing the EOS in a lower-density region are gradually constrained through terrestrial experiments, e.g., [2–9].

On the other hand, astronomical observations must be important for constraining the EOS in a higher-density region. For example, the discovery of the massive neutron stars, whose mass is $\sim 2M_\odot$, excluded the soft EOSs, with which the maximum mass does not reach the observed mass [10–13]. The observation of gravitational waves from GW170817 [14] could restrict the dimensionless tidal deformability of neutron stars, which leads to the constraint that the $1.4M_\odot$ neutron star radius should be less than 13.6 km [15]. In addition, through the observation of the pulsar light curve, one may constrain the neutron star properties, especially the stellar compactness, M/R, with stellar mass M and radius R, e.g., [16–21]. This is because the trajectory of the photon radiating from the neutron star's surface can bend due to the strong gravitational field induced by the neutron star, which is a relativistic effect. In practice, the Neutron star Interior Composition Explorer (NICER) is now operating on an International Space Station, which successfully constrained the neutron star mass and radius for PSR J0030-0451 [22,23] and for PSR J0740-6620 [24,25].

In such a way, the neutron star mass and radius would be constrained more and more in a higher density region with astronomical observations and in a lower density region with the terrestrial

experiments, e.g., [26–28] (also see Figure 1). Then, one may eventually constrain the EOS for neutron star matter.
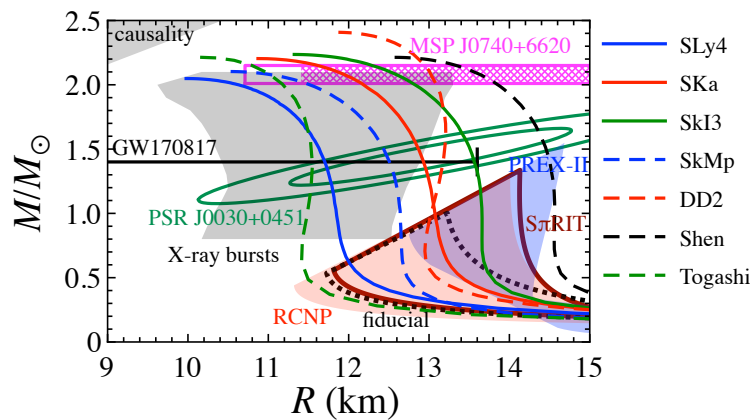

Figure 1. Several constraints on the neutron star mass and radius obtained from the astronomical observations and terrestrial experiments. MSP J0740+6620 is one of the massive neutron stars discovered up to now, whose mass is $M/M_\odot = 2.08 \pm 0.07$ [13], while the radius (and mass) of this object are also constrained via NICER as well as PSR J0030-0451. The tidal deformability restricted from the GW170817 event tells us the upper limit of the radius of $1.4M_\odot$ neutron star, i.e., $R_{1.4} \le 13.6$ km [15]. The observation of the X-ray bursts from neutron stars also gives us the constraint on the neutron star mass and radius, although they depend on the theoretical model [29]. In addition, one can theoretically exclude the top-left shaded region due to the causality [30]. On the other hand, the terrestrial experiments, e.g., by PREX-II [31], by SπRIT [32], and at RCNP [33], give us the constraint on the stellar models constructed with a lower central density (bottom-right region), adopting the mass formula for low-mass neutron stars [34], where the constraints expected with the fiducial value of the nuclear saturation parameters, i.e., $L = 60 \pm 20$ MeV [3,7,9] and $K_0 = 240 \pm 20$ MeV [2], is also shown (see Equation (1) for the definition of L and K_0). Furthermore, for reference, the mass and radius relations constructed with several EOSs are plotted. Taken from [26].

In addition to the observations (or estimations) of the neutron star mass and radius, the oscillation signals from neutron stars, if observed, are another important information to extract the neutron star properties. Since the objects have their own specific oscillation frequencies, one may know the interior information via the observation of their frequencies as an inverse problem. This technique is known as asteroseismology, which is similar to seismology on Earth and helioseismology on the Sun. In fact, the neutron star has a lot of oscillation modes, where each mode can be excited due to the corresponding physics. The gravitational waves from the neutron stars may be suitable astronomical information to adopt asteroseismology, but still, they have never been observed from an isolated neutron star. Even so, it has already been suggested that neutron star mass, radius, and EOS by observing the gravitational waves from the (cold) neutron stars, e.g., [35–45]. Moreover, this technique is also adopted for extracting the information of protoneutron stars from the supernova gravitational waves, e.g., [46–52].

Instead of the gravitational waves, the quasi-periodic oscillations (QPOs) discovered in the afterglow following the magnetar giant flares [53–59], are valuable information for adopting asteroseismology, where magnetars are strongly magnetized neutron stars. The observed QPO frequencies are in the range of tens of Hz up to kHz. Considering the dynamical time of neutron stars, it may be more difficult to theoretically explain the lower frequencies, and the possible candidates may be either crustal torsional oscillations or magnetic oscillations, if one assumes that the observed QPO frequencies come from the neutron star oscillations. However, the magnetic oscillations strongly depend on the magnetic field strength and its geometry inside the star, e.g., [60–62], while their understanding is quite poor. Thus, here we discuss the crustal properties by identifying the observed QPO frequencies

with the crustal torsional oscillations, neglecting magnetic effects. In this way, the crustal properties have been constrained indeed, e.g., [63–69].

Owing to the crust elasticity, the shear and interface modes are also excited as well as the torsional oscillations. Torsional oscillations are axial-type oscillations, while the shear and interface modes are polar-type oscillations. The precursors have been observed just before the main flare activity of gamma-ray burst at a binary neutron star merger [70], which may be a result of the resonant shattering of neutron star crusts induced by the binary orbital motion [71,72]. If so, one could extract the neutron star properties by carefully observing the precursors and identifying them with neutron star oscillations.

In this review, mainly focusing on the torsional oscillations excited in the neutron star, we extract the neutron star properties by identifying the observed QPO frequencies with the torsional oscillations. In addition, we examine the association of shear and interface modes with the neutron star properties. This manuscript is organized as follows. In Section 2, we shortly mention the observed QPO frequencies in magnetar giant flares, which will be considered as evidence of neutron star oscillations. In Section 3, we show the equilibrium neutron star models and the EOS considered in this study. In Section 4, we briefly mention the shear modulus inside the neutron star crust, which is an important property for considering the crustal oscillations. In Section 5, we extract the crustal information in practice by identifying the observed QPOs with the crustal torsional oscillations. In Section 6, we also show the behavior of the shear and interface modes, especially focusing on the association with the neutron star properties. Finally, we conclude in Section 7. Unless otherwise mentioned, we adopt geometric units in the following, $c = G = 1$, where c and G denote the speed of light and the gravitational constant, respectively.

2. Magnetar QPOs

Compared to usual pulsars whose surface magnetic field strength is $\sim 10^{12} - 10^{13}$ G, the existence of neutron stars with strong magnetic fields, such as $\sim 10^{14} - 10^{15}$ G, is observationally known. This strongly magnetized neutron star is known as a magnetar. In a rotating neutron star, the magnetic stress induced by the stellar rotation gradually accumulates in the crust, which is usually supported by crustal elasticity. But, once the magnetic stress becomes significantly strong and the crust elasticity cannot support it, the crust eventually breaks out, and the magnetic energy is released through the flare activities [73,74], where star quakes may also happen. This scenario could be the origin of the QPOs observed in the afterglow following the magnetar giant flares.

In practice, the QPOs have been discovered in the giant flares observed in soft-gamma repeaters (SGRs). In the events on SGR 1900+14 and SGR 1806-20, several QPOs are found [53–55], i.e., 28, 54, 84, and 155 Hz in SGR 1900+14, and 18, 26, 29 (or 30), 92.5, 150, 626.5, and 1837 Hz in SGR 1806-20. By a Bayesian analysis, the existence of additional QPOs was also reported in SGR 1806-20 [58]. Moreover, even without giant flares, the QPOs have been found from less energetic recurrent bursts, i.e., 93 and 127 Hz in SGR J1550-5418 [56], and 57 Hz in SGR 1806-20 [57]. In addition to the QPOs observed in the SGRs, several high QPO frequencies have been found in GRB 200415A, i.e., 836, 1444, 2132, and 4250 Hz [59].

Assuming that these QPOs come from neutron star oscillations, one may identify the higher QPO frequencies with polar perturbations of neutron stars, but the lower frequencies are more difficult to identify with neutron star oscillations. Maybe the possible candidates are only the crustal oscillations or magnetic oscillations (or magneto-elastic oscillations). Although the magnetic oscillations definitely depend on the geometry and strength of magnetic fields, which have not been fixed yet, it is pointed out that only crustal oscillations can be excited in the vicinity of the neutron star surface, while the magnetic oscillations are confined only to the core region, if magnetic fields are not so strong. The critical field strength, above which the magnetic oscillations become dominant, depends on the EOS (or crust properties), which is considered around a few times 10^{14} G [60,62,75]. So, to avoid the uncertainty

in the magnetic geometry and profile, assuming that the field strength is not so strong, we focus on only the crustal oscillations without magnetic effects in this review.

3. Crustal Equilibrium

Although the details of a neutron star structure depend on the EOS for neutron star matter, its conceptual structure is generally accepted. Under the thin envelope of the atmosphere and/or ocean, the matter forms a Coulomb lattice, which behaves as a solid. This region corresponds to the neutron star crust. Most of the crust region is composed of spherical nuclei with a bcc lattice, while the shape of stable nuclei changes into cylindrical, slablike, cylindrical-hole, and spherical-hole, and eventually becomes uniform matter, as density increases [76,77]. The region composed of non-spherical nuclei is the so-called pasta phase, which behaves as a liquid crystal. Meanwhile, the region whose density is higher than the transition density from the non-uniform to the uniform matter is the neutron star core. This transition density depends on the neutron star EOS, which becomes $\sim (1/3 - 1/2)$ of the nuclear saturation density. The transition density where the nuclear shape changes inside the crust also depends on the EOS, especially on the density dependence of the symmetry energy, L, in Equation (1) [78–80]. In addition, the crust thickness is at most 10% of the stellar radius, which depends on the stellar compactness, M/R, and the nuclear saturation parameters [77,81] (see Figure 2 for an example of the concrete stellar model). In general, the ratio of crust thickness to the stellar radius decreases as the stellar compactness and L increases. In particular, for $L \gtrsim 100$ MeV, the pasta phase disappears, where the crust is composed of only the spherical nuclei, and directly transitions into uniform matter [78–80] (also see Table 1).
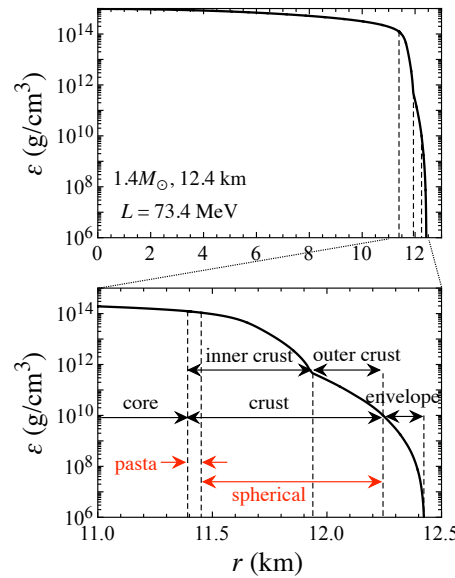

Figure 2. Example of the energy density profile inside the neutron star with $1.4 M_\odot$ and 12.4 km constructed with a specific EOS with $L = 73.4$ MeV and $K_0 = 230$ MeV, where L and K_0 are the nuclear saturation parameters given by Equation (1). The bottom panel is an enlarged view of the above panel. Taken from [82].

The EOS for neutron star matter generally depends on the adopted nuclear interaction, nuclear models, and the compositions. But for any EOSs, the bulk energy per baryon for the zero-temperature nuclear matter can be expanded in the vicinity of the saturation density, $n_0 \simeq 0.16$ fm^{-3}, of symmetric nuclear matter as a function of the baryon number density, n_b, and neutron excess, α, via [83]

$$\frac{E}{A} = w_0 + \frac{K_0}{2} u^2 + \mathcal{O}(u^3) + \left[S_0 + Lu + \mathcal{O}(u^2) \right] \alpha^2 + \mathcal{O}(\alpha^3), \tag{1}$$

where $u \equiv (n_b - n_0)/(3n_0)$, while n_b and α are given by $n_b = n_n + n_p$ and $\alpha = (n_n - n_p)/n_b$, using the neutron and proton number density, n_n and n_p. We note that the matter with $\alpha = 0$ corresponds to a symmetric nuclear matter, i.e. $n_n = n_p$, while that with $\alpha = 1$ is a pure neutron matter, i.e., $n_b = n_n$. The coefficients in this expansion are the nuclear saturation parameters, which characterize each EOS, and the term inside the brackets in front of α^2 corresponds to the nuclear symmetry energy.

Owing to the nature of the nuclear saturation properties, n_0, w_0, and S_0 are well determined via experiments, i.e., $n_0 \approx 0.15 - 0.16$ fm^{-3}, $w_0 \approx -15.8$ MeV [8], and $S_0 \approx 31.6 \pm 2.7$ MeV [9]. In contrast, K_0 and L are more difficult to determine experimentally, because they are a density derivative at $n_b = n_0$, i.e., one needs to know the nuclear information in a somewhat wide density range around the saturation point. Nevertheless, the constraints on these two parameters are improved, where their fiducial values are $K_0 = 230 \pm 40$ MeV [2,4] and $L \simeq 60 \pm 20$ MeV [3,7,9]. We note that the constraint on L still seems to have large uncertainties, e.g., $L = 106 \pm 37$ MeV with PREX-II done by the Thomas Jefferson National Accelerator Facility in Virginia [31], or $42 \le L \le 117$ MeV with SπRIT by Radioactive Isotope Beam Factory at RIKEN in Japan [32].

Anyway, in this review, to systematically discuss the dependence of the crustal oscillations on the nuclear saturation parameters, we especially adopt a phenomenological EOS proposed by Oyamatsu and Iida [78,79] (hereafter referred to as OI-EOS). For given values of K_0 and L, the OI-EOS family is constructed by optimizing the values of n_0, w_0, and S_0 to reproduce the experimental data for masses and charge radii of stable nuclei in such a way that the bulk energy reduces to Equation (1) in the limit of $n_b \to n_0$ and $\alpha \to 0$, adopting the extended Thomas-Fermi theory. The EOS parameters adopted in this review are listed in Table 1. We note that some of the EOS parameter sets are out of the range of fiducial values for K_0 and L, but we adopt such a wide range to systematically discuss the dependence on the saturation parameters.

Table 1. The EOS parameters for the OI-EOS family adopted in this review, where y is defined as $y \equiv -K_0 S_0/(3n_0 L)$. SP-C, C-S, S-CH, CH-SH, and SH-U denote the transition densities for each EOS parameter set. The asterisk at the value of K_0 denotes the EOS model with which some pasta phases are not predicted to appear, i.e., the values with $*1$, $*2$, and $*3$ denote the transition densities from cylindrical nuclei to uniform matter, from cylindrical-hole nuclei to uniform matter, and from spherical nuclei to uniform matter, respectively.

K_0 (MeV)	$-y$ (MeV fm^3)	L (MeV)	SP-C (fm^{-3})	C-S (fm^{-3})	S-CH (fm^{-3})	CH-SH (fm^{-3})	SH-U (fm^{-3})
180	1800	5.7	0.06000	0.08665	0.12039	0.12925	0.13489
180	600	17.5	0.05849	0.07986	0.09811	0.10206	0.10321
180	350	31.0	0.05887	0.07629	0.08739	0.09000	0.09068
180	220	52.2	0.06000	0.07186	0.07733	0.07885	0.07899
230	1800	7.6	0.05816	0.08355	0.11440	0.12364	0.12736
230	600	23.7	0.05957	0.07997	0.09515	0.09817	0.09866
230	350	42.6	0.06238	0.07671	0.08411	0.08604	0.08637
230	220	73.4	0.06421	0.07099	0.07284	0.07344	0.07345
280	1800	9.6	0.05747	0.08224	0.11106	0.11793	0.12286
280	600	30.1	0.06218	0.08108	0.09371	0.09577	0.09623
280	350	54.9	0.06638	0.07743	0.08187	0.08314	0.08331
*280	220	97.5	0.06678	—	—	—	0.06887^{*1}
360	1800	12.8	0.05777	0.08217	0.10892	0.11477	0.11812
360	600	40.9	0.06743	0.08318	0.09197	0.09379	0.09414
*360	350	76.4	0.07239	0.07797	0.07890	—	0.07918^{*2}
*360	220	146.1	—	—	—	—	0.06680^{*3}

As an equilibrium crust model (or a neutron star model), we simply consider a non-rotating, strain-free, and spherically symmetric neutron star model in this review. The metric describing such a stellar model is given by

$$ds^2 = -e^{2\Phi}dt^2 + e^{2\Lambda}dr^2 + r^2(d\theta^2 + \sin^2\theta d\phi^2), \tag{2}$$

where Φ and Λ are the metric functions depending on only the radial coordinate, r. Λ is directly associated with the mass function, $m(r)$, which corresponds to the enclosed gravitational mass inside the position r, i.e., $e^{-2\Lambda} = 1 - 2m/r$. Adopting an appropriate EOS, e.g., the OI-EOS family in this review, one can construct the stellar model by integrating the Tolman-Oppenheimer-Volkoff (TOV) equation. In general, to construct a stellar model, one integrates the TOV equation outward from the center to the surface, assuming a central density, i.e., the neutron star models become one parameter family for each EOS. In fact, we construct the stellar model in this way for discussing the shear and interface modes in Section 6, because these modes are polar-type oscillations, which are excited not only in the crust region but also inside the core. On the other hand, the torsional oscillations discussed in Section 5, which are axial-type oscillations, are confined inside the crust (elastic) region. So, to remove the uncertainties of the core EOS, we construct only the crust equilibrium for discussing the torsional oscillations, where we integrate the TOV equations inward from the stellar surface to the base of the crust, assuming the stellar mass and radius as a boundary condition at the stellar surface.

4. Shear Modulus

The elasticity inside the crust can be characterized by the shear modulus, μ. The shear modulus, μ_{sp}, in a phase of spherical nuclei with a bcc lattice is approximately described in the limit of zero-temperature as

$$\mu_{sp} = 0.1194 \frac{n_i (Ze)^2}{a}, \tag{3}$$

where n_i, Z, and a are the ion number density, charge number of the ion, and Wigner-Seitz cell radius, i.e., $4\pi a^3/3 = 1/n_i$ [84]. This expression has been derived by averaging the overall direction, assuming that each nuclei is only a point-particle [85]. The shear modulus in the phase of spherical nuclei has been discussed more by including the phonon contribution [86], the electron-screening effect [87,88,103], the effect of polycrystal properties [89], and effects of finite size of atomic nuclei [90], which can modify the shear modulus more or less. But, in this review, we simply adopt μ_{sp} given by Equation (3) as shear modulus in the phase of spherical nuclei.

Compared to the shear modulus in the phase of spherical nuclei, the discussion for the shear modulus in the pasta phases is very poor. Nevertheless, according to Ref. [91], the shear modulus, μ_{cy}, in the phase of cylindrical nuclei can be estimated as

$$\mu_{cy} = \frac{2}{3} E_{\text{Coul}} \times 10^{2.1(w_2 - 0.3)}, \tag{4}$$

where E_{Coul} and w_2 denote the Coulomb energy per volume of a Wigner-Seitz cell and the volume fraction of cylindrical nuclei, while the shear modulus, μ_{sl}, in the phase of slablike nuclei is

$$\mu_{sl} = 0, \tag{5}$$

i.e., the matter composed of slablike nuclei behaves as a fluid within the linear response. This is because the deformation energy in slablike nuclei becomes of higher order with respect to the displacement [91]. So, in this review we simply adopt Equations (4) and (5) as the shear modulus in the phases of cylindrical and slablike nuclei. But, on the other hand, it has been also suggested that the elastic constant in the poly-crystalline lasagna (which corresponds to slablike nuclei) may become a (nonzero) tiny value [92,93]. If one considers the nonzero shear modulus inside the slablike nuclei, the results shown in this review may be changed.

Furthermore, the shear modulus in the phase of cylindrical-hole, μ_{ch}, and spherical-hole nuclei, μ_{sh}, may be considered in a similar way to that in the phase of cylindrical and spherical nuclei. This is because the liquid crystalline structures in the phase of cylindrical-hole and spherical-hole nuclei are basically the same as in the phase of cylindrical and spherical nuclei. Thus, we adopt Equations (4) and (3) for μ_{ch} and μ_{sh} by appropriately replacing the quantities in the formulae [69,94]. That is, w_2 in

Equation (4) is replaced by the volume fraction of gas of dripped neutron for μ_{ch}, while n_i and Z in Equation (3) are replaced by the number density of spherical-holes (bubbles) and the effective charge number, Z_{sh}, of spherical-hole for μ_{sh}, where Z_{sh} is estimated as $Z_{sh} = n_Q V_{sh}$ with the effective charge number density of the spherical-hole, n_Q, and the volume of the spherical-hole, V_{sh}. n_Q is given by the difference of the charge number density inside the spherical-hole from that outside the spherical-hole, i.e., $n_Q = -n_e - (n_p - n_e) = -n_p$, using the proton number density outside the spherical-hole, n_p, and the number density of uniform electron gas, n_e.

In Figure 3, we show an example of the distribution of shear modulus inside the crust for the stellar model shown in Figure 2, where the right panel is an enlarged view of the shaded region in the left panel.
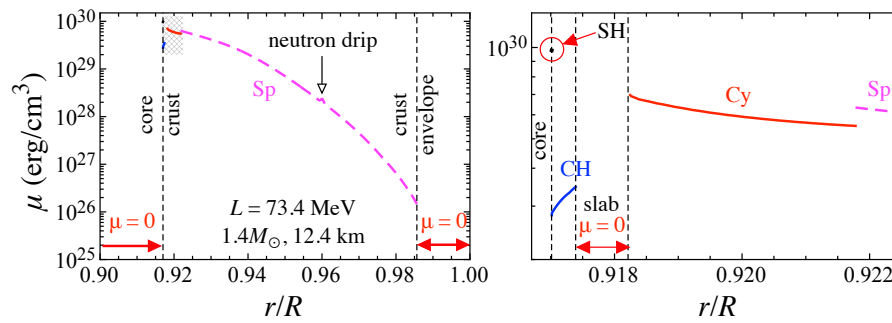

Figure 3. Shear modulus inside the neutron star model given by Figure 2, where Sp, Cy, CH, and SH respectively denote the phases composed of spherical, cylindrical, cylindrical-hole, and spherical-hole nuclei. The right panel is an enlarged view of the shaded region in the left panel. Taken from [82].

5. Crustal Torsional Oscillations

On the crustal equilibrium models mentioned in the previous section, we make a linear perturbation analysis to determine the specific frequencies of crustal torsional oscillations. For this purpose, we simply adopt the Cowling approximation, where the metric perturbation is neglected during the fluid oscillations. The perturbation equation can be derived from the linearized energy-momentum conservation law. In practice, introducing the ϕ-component of the Lagrangian displacement, $\xi^\phi = \mathcal{Y}(r)e^{i\omega t}\partial_\theta P_\ell(\cos\theta) / \sin\theta$, where $P_\ell(\cos\theta)$ denotes the ℓ-th order Legendre polynomial, the perturbation equation becomes [60,95]

$$\mathcal{Y}'' + \left[\left(\frac{4}{r} + \Phi' - \Lambda'\right) + \frac{\mu'}{\mu}\right]\mathcal{Y}' + \left[\frac{\tilde{H}}{\mu}\omega^2 e^{-2\Phi} - \frac{(\ell+2)(\ell-1)}{r^2}\right]e^{2\Lambda}\mathcal{Y} = 0, \tag{6}$$

where the dash denotes the derivative with r and $\tilde{H}$ denotes the effective enthalpy contributing the oscillations, given by

$$\tilde{H} = \left(1 - \frac{N_s}{A}\right)H \tag{7}$$

for the spherical or cylindrical nuclei [66,96], while

$$\tilde{H} = \frac{N_i + \mathcal{R}(A - N_i)}{A}H \tag{8}$$

for the cylindrical-hole or spherical-hole nuclei [69].

In the expression of the effective enthalpy, H denotes the local enthalpy given by $H = \varepsilon + p$ with the energy density, ε, and pressure, p, while A is the baryon number density inside a Wingner-Seitz cell, N_s is the number of neutrons inside a Wingner-Seitz cell that do not comove with protons in the nuclei, N_i is the number of neutrons inside a cylindrical-hole or spherical-hole, and $\mathcal{R}$ is a parameter characterizing a participant ratio in the oscillations, i.e., how much ratio of nucleons outside the

cylindrical-hole or spherical-hole comove with it non-dissipatively. That is, all the nucleons inside a Wingner-Seitz cell contribute to the effective enthalpy with $\mathcal{R} = 1$ (maximum enthalpy), while no nucleons outside the cylindrical-hole or spherical-hole do so with $\mathcal{R} = 0$ (minimum enthalpy). We note that $\mathcal{R}$ in a phase of spherical-hole nuclei is predicted as $\sim 0.34 - 0.38$ at $n_b = 0.08$ fm^{-3} from the band calculations [97]. Meanwhile, assuming that N_s comes only from a part of the dripped neutrons inside a Wingner-Seitz cell, N_d, the parameter N_s/N_d can control the fraction of neutrons contributing to the oscillations, i.e., $N_s/N_d = 0$ corresponds to the situation that all the dripped neutrons comove with the protons (maximum enthalpy), while $N_s/N_d = 1$ is that all the dripped neutrons behave as a superfluid and do not contribute to the oscillations (minimum enthalpy).

To determine the frequencies, one has to impose appropriate boundary conditions in the perturbation equation (6) at the basis of the crust (the boundary between the core and crust) and the surface of the crust (or the boundary between the crust and envelope). Both boundaries are essentially equivalent to the boundary between the elastic and fluid region, where we impose the condition that the traction force vanishes [60,95], which reduces to $\mathcal{Y}' = 0$. On the other hand, at the interface between the elastic regions with different shapes of nuclei, e.g., between the spherical and cylindrical nuclei, we impose a continuous traction condition, i.e., $\mu \mathcal{Y}'$ should be continuous at such an interface. Then, the problem to solve becomes an eigenvalue problem with respect to the eigenvalue, ω. The resultant value of ω gives us the frequency, f, via $f = \omega/2\pi$ for each value of ℓ. In this review, we use the notation of $_n t_\ell$ for expressing the eigenfrequencies of torsional oscillations with the angular index ℓ and the nodal number in the eigenfunction (although the notation is different from the usual one, such as $_\ell t_n$).

5.1. Torsional Oscillations Excited in the Spherical Nuclei

Even though the crust is not only composed of the spherical nuclei as mentioned above, to see the dependence of the frequencies of the torsional oscillations on the EOS parameters and stellar properties, first we consider the torsional oscillations excited in the elastic region composed of only the spherical nuclei. As a first step, we examine the frequencies without neutron superfluidity, i.e., $N_s/N_d = 0$ (or $\tilde{H} = H$). As mentioned in Section 3, to construct the equilibrium model, we have to select two parameters for EOS, i.e., K_0 and L, and two for stellar models, M and R. In the left panel of Figure 4, we show the fundamental frequencies of $\ell = 2$ torsional oscillations for a neutron star model with $1.4M_\odot$ and 12 km, using the EOSs with some parameter sets listed in Table 1 (see Ref. [67] for the concrete parameter sets adopted here), as a function of L. From this figure, one can observe that the frequencies are less sensitive to K_0. Thus, we will discuss the dependence of the fundamental frequency as a function of L through the fitting formula by assuming the polynomial form as

$$_0 t_2 = c_2^{(0)} + c_2^{(1)} L_{100} + c_2^{(2)} L_{100}^2 \tag{9}$$

where $c_2^{(i)}$ with $i = 0, 1, 2$ are the adjustable parameters depending on M and R (and N_s/N_d), while L_{100} is the value of L normalized by 100 MeV. Using this fitting formula, one can estimate the frequency of $_0 t_2$ less than $\sim 5\%$ accuracy for a neutron star model with $1.4M_\odot$ and 12 km (Table 2 in [67]). In the left panel of Figure 4, we also show the expected frequencies with the fitting formula given by Equation (9) by the thick-solid line.

One may be able to understand the dependence of $_0 t_2$ on L as follows. As the value of L increases, the nuclear symmetry energy conversely decreases at the sub-nuclear density, considering the density dependence of the bulk energy given by Equation (1). As a result, protons easily turn into neutrons, which leads to the situation that the charge number of nuclei gets smaller. This means that μ_{sp} becomes smaller from Equation (3). On the other hand, the fundamental frequency of the ℓ-th torsional oscillations, $_0 t_\ell$, are estimated as $_0 t_\ell \sim [\ell(\ell+1)]^{1/2} v_s/R$ with the shear velocity, $v_s \equiv (\mu/\tilde{H})^{1/2}$ [101]. Thus, one can expect that $_0 t_\ell$ decreases with L.

Now, assuming the neutron star mass and radius would be in the range of $1.4 \le M/M_\odot \le 1.8$ and 10 km $\le R \le 14$ km, which are reasonable assumptions as a neutron star model, the resultant

fundamental frequency of the $\ell = 2$ torsional oscillations is shifted, depending on the stellar models. In the right panel of Figure 4, we show the expected region of $_0t_2$ for such neutron star models as a function of L. We note that $_0t_2$ decreases with R and M. So, the lower bound of the shaded region corresponds to the stellar model with $1.8M_\odot$ and 14 km. On the other hand, the lowest QPO frequency observed in the SGR 1806-20, i.e., 18 Hz, is also shown in the right panel of Figure 4. Since the $\ell = 2$ fundamental torsional oscillations are theoretically the lowest frequency among a lot of eigenfrequencies of the torsional oscillations, $_0t_2$ should be equal to or even lower than the observed lowest QPO frequency on the assumption that the magnetar QPOs come from the crustal torsional oscillations. Then, from the right panel of Figure 4, one can get the constraint on L as $L \gtrsim 47.4$ MeV, if the central object of SGR 1806-20 is a neutron star with $M \leq 1.8M_\odot$ and $R \leq 14$ km [65,67]. Similarly, if the central object is a typical neutron star with $1.4M_\odot$ and 10 km, L is constrained as $L \simeq 76.2$ MeV.
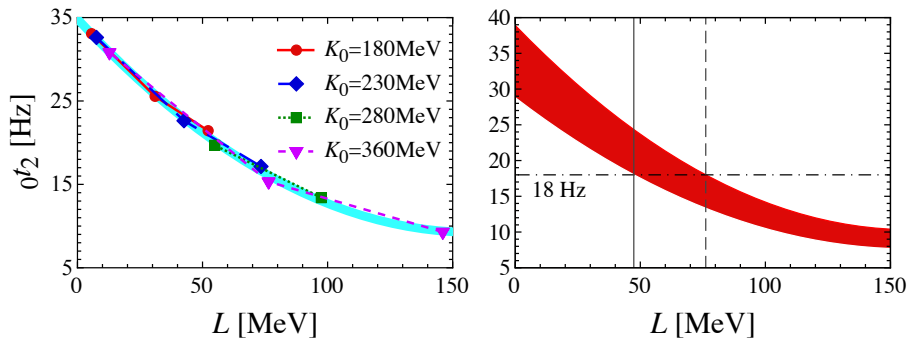

Figure 4. In the left panel, the fundamental frequencies of $\ell = 2$ torsional oscillations for a neutron star model with $1.4M_\odot$ and 12 km constructed with several EOS parameter sets are shown as a function of L. The thick-solid line is the expected frequency using the fitting formula given by Equation (9). In the right panel, the expected fundamental frequency of $\ell = 2$ torsional oscillations as a function of L, assuming that the neutron star mass and radius are in the range of $1.4 \leq M/M_\odot \leq 1.8$ and 10 km $\leq R \leq 14$ km, where for reference the lowest QPO frequency observed in SGR 1806-20, i.e., 18 Hz, is also shown. The vertical solid and broken lines correspond to $L = 47.4$ and 76.2 MeV, respectively. Taken from [67].

Next, we take into account neutron superfluidity in the crustal torsional oscillations, i.e., $N_s/N_d \neq 0$. To see how the frequencies depend on N_s/N_d, we calculate $_0t_2$, assuming that N_s/N_d is constant inside the inner crust. We confirm that $_0t_2$ for a given neutron star model can be well expressed as a function of L using Equation (9) even for $N_s/N_d \neq 0$. In Figure 5, we show the L dependence of $_0t_2$ for a neutron star model with $1.8M_\odot$ and 14 km as varying the ratio of N_s/N_d with each 0.2 from 0 to 1 (the solid lines from bottom to top). The tendency of why the frequency increases with N_s/N_d can also be understood with the dependence of frequency on the shear velocity. As mentioned above, the effective enthalpy, $\tilde{H}$, decreases with N_s/N_d, which leads to the increase of the shear velocity. So, as a result, one can expect that the frequency also increases since $_0t_\ell \sim v_s$. We note that the neutron star model discussed for the L dependence of $_0t_2$ in Figure 5 corresponds to the stellar model, which gives the lower boundary of the shaded region in Figure 4. That is, assuming that the central object in SGR 1806-20 is a neutron star with $M \leq 1.8M_\odot$ and $R \leq 14$ km, and also assuming that the lowest QPO frequency observed in SGR 1806-20 comes from $_0t_2$, one can get the constraint on L as $L \gtrsim L_{min}$ with the lower limit of L_{min}, depending on N_s/N_d, where L_{min} is determined as the intersection of the L dependence of $_0t_2$ and 18 Hz (dot-dashed line) in Figure 5, i.e., L_{min} increases with N_s/N_d [66].

In a realistic stellar model, N_s/N_d should depend on the density. According to the band calculations in [97], the ratio of N_s/N_d is only of the order of $10 - 30$ percent at $n_b \sim 0.01 - 0.4n_0$, even though the ratio of N_s/N_d is still under debate, e.g., [98–100]. The fundamental frequencies determined with this density dependence of N_s/N_d are also shown in Figure 5 with marks (and the dashed line for their fitting), which are close to the results obtained with $N_s/N_d = 0.2$. Anyway, since the frequencies of

torsional oscillations strongly depend on the ratio of N_s/N_d, it is quite important to understand the ratio of N_s/N_d in a realistic situation.
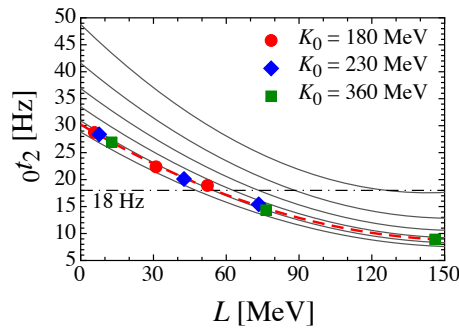

Figure 5. For a neutron star model with $1.8M_\odot$ and 14 km, the fundamental frequency of $\ell = 2$ torsional oscillations is plotted as a function of L, as changing the ratio of N_s/N_d with each 0.2 from 0 to 1, where N_s/N_d is assumed to be constant inside the inner crust. Meanwhile, the marks denote the frequencies, using the density-dependent N_s/N_d derived in [97], and the dashed line is their fitting with Equation (9). Taken from [66].

In a similar way to the fundamental frequencies of the $\ell = 2$ torsional oscillations, one can discuss the L dependence of the ℓ-th torsional oscillations. Actually, if one systematically examines the frequencies, one can find that $_0t_\ell$ is also well fitted as a function of L, which weakly depends on K_0, as

$$_0t_\ell = c_\ell^{(0)} + c_\ell^{(1)} L_{100} + c_\ell^{(2)} L_{100}^2,\qquad(10)$$

where $c_\ell^{(i)}$ with $i = 0, 1, 2$ are also the adjustable parameters depending on M and R (and N_s/N_d) [66]. Using this L dependence of $_0t_\ell$, we will discuss the QPO frequencies observed in SGR 1806-20 and 1900+14, even though one should also consider the effect of the existence of pasta (see Sections 5.2 and 5.3, and also [102]). In Figure 6, we show the fundamental frequencies of torsional oscillations with specific values of ℓ for a neutron star model with $1.4M_\odot$ and 12 km, adopting the results in [97] for N_s/N_d. From the left panel one can observe that the 18, 26, 30, and 92.5Hz QPOs in SGR 1806-20 are well identified with $\ell = 3, 4, 5, 15$ fundamental oscillations if $L \simeq 128.0$ MeV, while from the right panel one can observe that the 28, 54, and 84 Hz QPOs in SGR 1900+14 are with $\ell = 4, 8, 13$ fundamental oscillations if $L \simeq 113.5$ MeV. We note that the other low-lying QPO frequencies discovered later can also be identified with the torsional oscillations with different values of ℓ in the same framework [69,96,103] (also see Section 5.2 and 5.3).
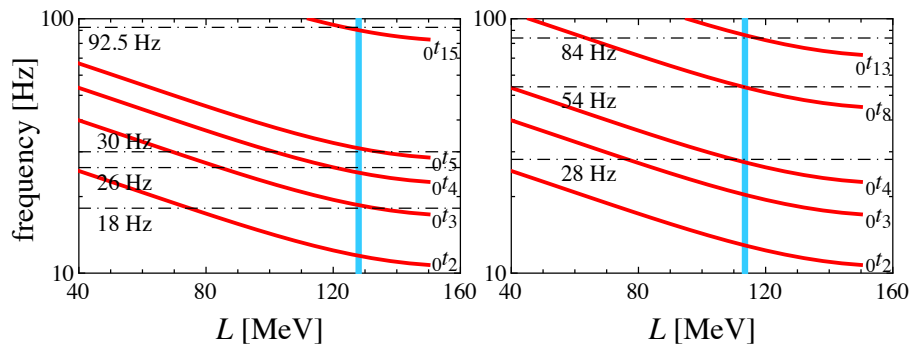

Figure 6. The fundamental frequencies of the torsional oscillations with several values of ℓ for a neutron star model with $1.4M_\odot$ and 12 km are shown as a function of L. The QPO frequencies observed in SGR 1806-20 and SGR 1900+14 are compared with them in the left and right panels. Taken from [67].

Since the neutron star mass and radius in SGR 1806-20 and SGR 1900+14 are not constrained, it may be better to consider the stellar models with a typical range of mass and radius. In practice, if the stellar mass and radius are changed in a certain range, the resultant L dependence of $_0t_\ell$ are shifted up and down in Figure 6 with the same combination of the ℓ-th oscillations. As a result, the optimal value of L, with which the QPOs observed in SGRs are well identified with the torsional oscillations, is also shifted left and right. In the left panel of Figure 7, the optimal values of L, with which the QPO frequencies observed in SGR 1806-20 (with filled marks) and in SGR 1900+14 (with open marks) are well identified as shown in Figure 6, are shown for various neutron star models. From this figure, one can see that L should be in the range of $101.1 \lesssim L \lesssim 160.0$ MeV for explaining SGR 1806-20 and $90.5 \lesssim L \lesssim 131.0$ MeV for explaining SGR 1900+14, if the central objects of both SGRs are a neutron star with $1.4 \leq M/M_\odot \leq 1.8$ and 10 km $\leq R \leq 14$ km. Meanwhile, since the value of L should be universal, i.e., independent of the astronomical events, one has to simultaneously explain both events, SGR 1806-20 and SGR 1900+14, with the same value of L. Thus, we get a more stringent constraint on L, i.e., $101.1 \lesssim L \lesssim 131.0$ MeV [67], which are shown in the left panel of Figure 7 with the shaded region. Furthermore, since the symmetry energy at $n_b = n_0$, S_0, is approximately estimated as a function of L [78] through

$$S_0 \approx 28 \text{ MeV} + 0.075L, \tag{11}$$

one can constrain S_0 to explain the QPOs observed in the SGRs as $35.6 \lesssim S_0 \lesssim 37.8$ MeV.
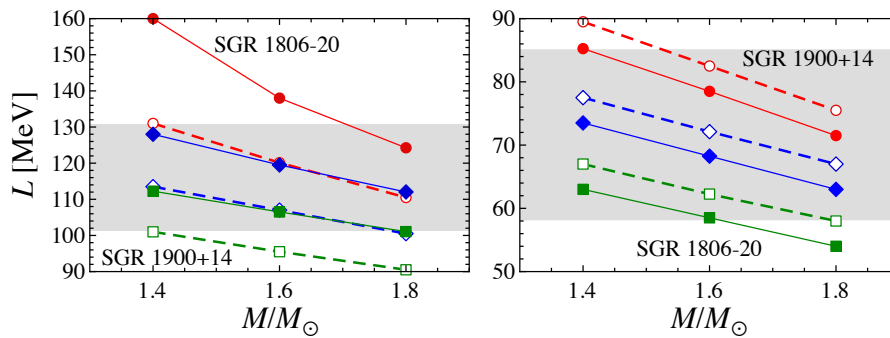

Figure 7. The values of L, with which the QPOs observed in SGR 1806-20 (SGR 1900+14) are well identified by the fundamental torsional oscillations, are shown with filled marks with solid lines (open marks with dashed lines) for different neutron star models, i.e., the circles, diamonds, and squares correspond to the stellar models with 10, 12, and 14 km radius. The left and right panels correspond to the identification shown in Figure 6 and 8, respectively. The shaded region is the constraint on L, with which the QPOs observed in both SGR 1806-20 and 1900+14 are simultaneously explained by the torsional oscillations. Taken from [67].

On the other hand, considering the constraints on L obtained from terrestrial experiments whose fiducial value is $L \simeq 60 \pm 20$ MeV [3,7,9], the resultant constraint on L may be too large, although a larger value of L has also been reported [31,32]. So, if any, it may be better to consider an alternative possible correspondence to explain the QPO frequencies observed in the SGRs with the fundamental torsional oscillations. As an alternative possible correspondence, we find that the 18, 30, and 92.5 Hz QPOs in SGR 1806-20 are identified with the $\ell = 2, 3, 10$ fundamental torsional oscillations, while the 28, 54, and 84 Hz in SGR 1900+14 are with the $\ell = 3, 6, 9$ oscillations, as shown in Figure 8 for a neutron star model with $1.4M_\odot$ and 12 km, where the value of L should be $L \simeq 73.5$ MeV in SGR 1806-20 and $L \simeq 77.5$ MeV in 1900+14. We note that the 26 Hz QPO in SGR 1806-20 cannot be identified with this correspondence (see Section 5.3 for this missing identification). Considering a typical neutron star model with $1.4 \leq M/M_\odot \leq 1.8$ and 10 km $\leq R \leq 14$ km, one can get the optimal values of L as shown in the right panel of Figure 7. To simultaneously explain the QPOs observed in the SGRs, we obtain the constraint on L as $58.0 \lesssim L \lesssim 85.3$ MeV (shaded region in the right panel), assuming that the central

object in the SGR 1806-20 and SGR 1900+14 is a neutron star with $1.4 \leq M/M_\odot \leq 1.8$ and 10 km $\leq R \leq 14$ km [67]. This constraint on L additionally gives us the constraint on S_0 as $32.4 \lesssim S_0 \lesssim 34.4$ MeV, using Equation (11). We note that the fundamental frequencies of ℓ-th torsional oscillations excited inside the phase of spherical nuclei can be expressed as a function of ℓ, L, stellar mass, and radius [104].
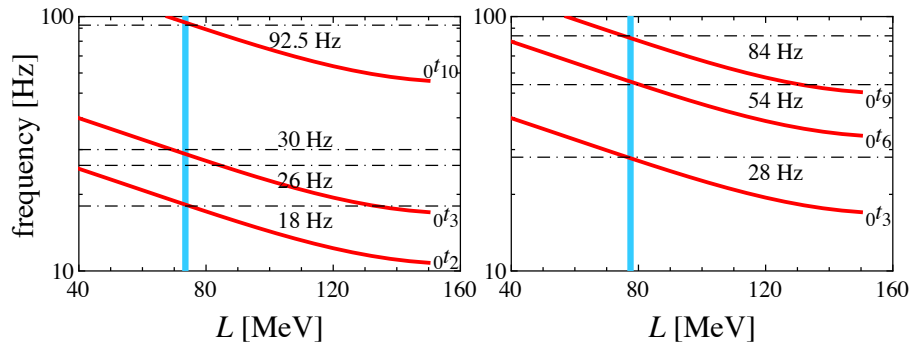

Figure 8. Alternative possible correspondence of the QPO frequencies observed in SGR 1806-20 (left panel) and SGR 1900+14 (right panel) with the fundamental torsional oscillations for a neutron star model with $1.4 M_\odot$ and 12 km. Taken from [67].

5.2. Torsional Oscillations Excited in the Spherical and Cylindrical Nuclei

Since in this review we simply consider that the shear modulus inside the phase of slablike nuclei is zero, as mentioned in Section 4, the torsional oscillations in the region composed of spherical and cylindrical nuclei can be excited independently from those in the region composed of cylindrical-hole and spherical-hole nuclei. That is, torsional oscillations are excited independently in two layers across the phase of slablike (lasagna) nuclei as "a lasagna sandwich" [69]. In this subsection, we discuss the torsional oscillations excited in the outer layer, i.e., the phase of spherical and cylindrical nuclei, while those excited in the inner layer, i.e., the phase of cylindrical-hole and spherical-hole nuclei, will be discussed in the next subsection (Section 5.3).

Unlike the phase of spherical nuclei, the understanding of the ratio of N_s/N_d in the phase of cylindrical nuclei is poor. So, we simply consider the extreme case, i.e., $N_s/N_d = 0$ and 1 in the phase of cylindrical nuclei. On the other hand, we adopt the result obtained in [97] for N_s/N_d in the phase of spherical nuclei, as in the previous subsection. Then, one can determine the frequencies of torsional oscillations by solving an eigenvalue problem.

To see how the frequency of the torsional oscillation changes due to the existence of cylindrical nuclei, in Figure 9, we show $_0t_2$ as a function of L for a neutron star model with $1.4 M_\odot$ and 12 km, using the EOSs with some parameter sets listed in Table 1 (see Ref. [96] for the concrete parameter sets adopted here), where the left and right panels correspond to the results with $N_s/N_d = 0$ and 1, respectively, and the thick-solid line is the fitting with Equation (9). For reference, we also show the L dependence of $_0t_2$ excited in the phase of only spherical nuclei discussed in Section 5.1 with the dashed line. From this figure, one can observe that the modification in $_0t_2$ due to the existence of cylindrical nuclei appears only for a neutron star model with a lower value of L. This is because the phase of cylindrical nuclei as well as the other pasta phases becomes narrower with L [78–80], i.e., one can neglect the existence of cylindrical nuclei in the stellar model with larger L. In any case, the fundamental torsional oscillations hardly depend on K_0 and one can discuss the L dependence through the fitting given by Equation (10).
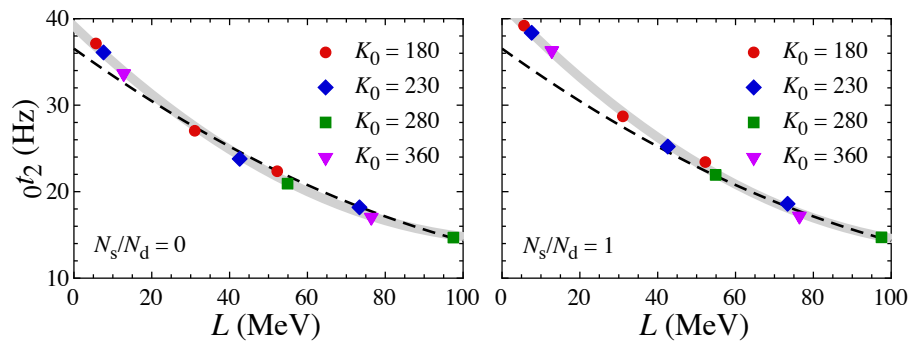
Figure 9. The fundamental frequencies of the $\ell = 2$ torsional oscillations excited in the phase of spherical and cylindrical nuclei for a neutron star model with $1.4M_\odot$ and 12 km are shown with various marks. The left and right panels are results with $N_s/N_d = 0$ and 1, respectively. The thick-solid line denotes the fitting with Equation (9), while the dashed line denotes the L dependence of $_0t_2$ exited in the phase of only spherical nuclei discussed in Section 5.1. Taken from [96].

Using the L dependence of $_0t_\ell$ with $N_s/N_d = 1$ in the phase of cylindrical nuclei, in Figure 10, we compare the fundamental torsional oscillations with various ℓ for a neutron star model with $1.4M_\odot$ and 12 km to the low-lying QPO frequencies observed in SGR 1806-20 (left panel) and SGR 1900+14 (right panel), where the horizontal dashed and dotted lines denote the observed QPO frequencies and the solid lines denote the L dependence of $_0t_\ell$. We note that we focus on only the correspondence of the observed low-lying QPOs except for the 26 Hz QPO in SGR 1806-20 here, because the optimal value of L becomes larger than 100 MeV to identify all the observed low-frequency QPOs in terms of the crustal torsional oscillations, as discussed in Section 5.1, which may be inconsistent with the constraint from existing nuclear experiments. We also note that the 57 Hz QPO additionally discovered in [57] is taken into account this time. From this figure, one sees that the observed QPOs (except for the 26 Hz QPO) in SGR 1806-20 can be identified if $L \simeq 73.4$ MeV, and those in SGR 1900+14 can be identified if $L \simeq 76.1$ MeV.
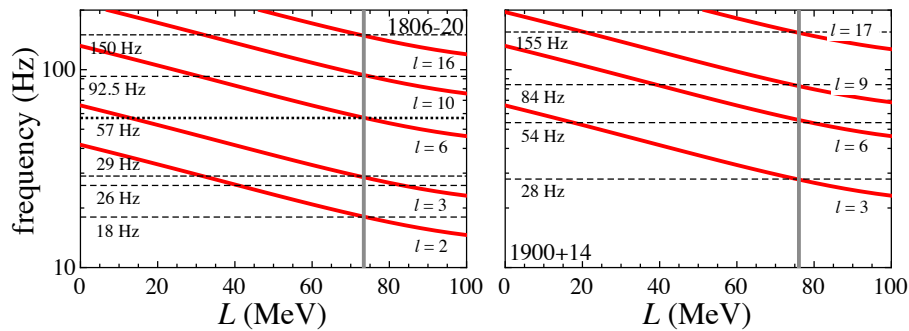

Figure 10. Correspondence of the low-lying QPO frequencies (except for the 26 Hz QPO) observed in SGR 1806-20 (left panel) and 1900+14 (right panel) with the several fundamental torsional oscillations for a neutron star model with $1.4M_\odot$ and 12 km, assuming that $N_s/N_d = 1$ in the phase of cylindrical phase. Taken from [96].

Similarly, one can determine the optimal value of L to identify the observed QPOs with the same set of the fundamental torsional oscillations shown in Figure 10 for various neutron star models with $N_s/N_d = 0$ and 1 in the phase of cylindrical nuclei. Assuming that $1.4 \le M/M_\odot \le 1.8$ and 10 km $\le R \le 14$ km as a typical neutron star model, the optimal value of L for identifying the QPO frequencies observed in the SGRs with the same correspondence as shown in Figure 10, are plotted in Figure 11 for $N_s/N_d = 0$ in the left panel and $N_s/N_d = 1$ in the right panel. In this figure, the filled marks with solid lines correspond to the resultant values of L for SGR 1806-20, while the open marks

with dashed lines are for SGR 1900+14. Again, since the value of L should be independent of the astronomical events, one has to simultaneously explain both events, SGR 1806-20 and SGR 1900+14, with a specific value of L. Thus, we can get the constraint on L as $53.9 \lesssim L \lesssim 83.6$ MeV for $N_s/N_d = 0$ and $58.1 \lesssim L \lesssim 85.1$ MeV for $N_s/N_d = 1$, assuming that the central object of SGR 1806-20 and SGR 1900+14 is a neutron star with $1.4 \leq M/M_\odot \leq 1.8$ and 10 km $\leq R \leq 14$ km. These constraints on L are shown with the shaded region in Figure 11. Namely, the uncertainty in N_s/N_d in the phase of cylindrical nuclei makes only a little difference in the constraint on L, where the allowed L lies in the range of $L = 53.9 - 85.1$ MeV, even if the uncertainty in N_s/N_d in the phase of cylindrical nuclei is taken into account. This constraint on L gives us the constraint of S_0 as $S_0 \simeq 32.0 - 34.4$ MeV, using the correlation between L and S_0 given by Equation (11).
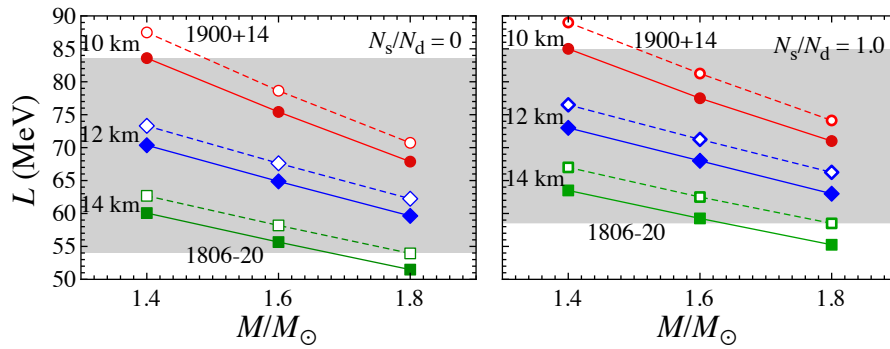

Figure 11. The optimal value of L for identifying the low-lying QPO frequencies (except for the 26 Hz QPO) observed in SGR 1806-20 (filled marks with solid lines) and SGR 1900+14 (open marks with dashed lines) for various neutron star models, where the left and right panels are the results with $N_s/N_d = 0$ and 1, respectively. Taken from [96].

On the other hand, since the torsional oscillations are confined inside the phase of spherical and cylindrical nuclei, we can also discuss the overtone(s) of torsional oscillations. The n-th overtone frequencies of the ℓ-th torsional oscillations, $_nt_\ell$, is theoretically estimated with the crust thickness (or the thickness of elastic region), ΔR, as $_nt_\ell \sim v_s/\Delta R$ [101]. Meanwhile, ΔR depends on the EOS parameters L and K_0 mainly through the neutron chemical potential at the crust–core boundary [81], when the neutron star mass and radius are fixed. Thus, via the identification of the relatively high-frequency QPO observed in SGR 1806–20, i.e., 626.5 Hz, as the 1st overtone of crustal torsional oscillations, one may obtain information about the EOS parameters [65,96].

Since $_nt_\ell$ depends on K_0 and L through ΔR, it is of great use to find a parameter constructed by a combination of K_0 and L, which can characterize $_nt_\ell$. To this end, assuming the combination of $(K_0^i L^j)^{1/(i+j)}$ with integer numbers i and j, we finally find an appropriate combination of K_0 and L as

$$\varsigma \equiv (K_0^4 L^5)^{1/9}. \tag{12}$$

In Figure 12, we show the 1st overtones of $\ell = 2$ torsional oscillations for a neutron star model with $1.4M_\odot$ and 12 km constructed with various EOS parameters, where the thick-solid line denotes the fitting formula for the 1st overtones of the torsional oscillations given by [75,96]

$$_nt_\ell = d_{\ell n}^{(0)} + d_{\ell n}^{(1)}\varsigma + d_{\ell n}^{(2)}\varsigma^2, \tag{13}$$

where $d_{\ell n}^{(i)}$ for $i = 0, 1, 2$ are the adjustable parameters depending on M, R, and N_s/N_d in the phase of cylindrical nuclei. We will, hereafter, discuss the ς dependence of $_nt_\ell$.
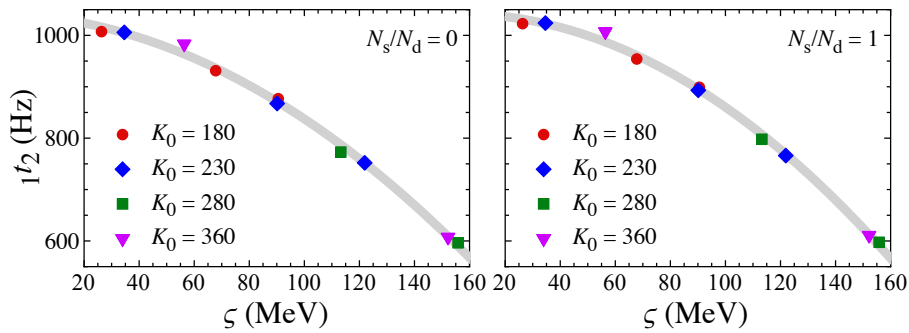
Figure 12. The 1st overtones of $\ell = 2$ torsional oscillations for a neutron star model with $1.4 M_\odot$ and 12 km constructed with various EOS parameters are shown as a function of ς defined by Equation (12), where the left and right panels respectively denote the results with $N_s/N_d = 0$ and 1 in the phase of cylindrical nuclei. The thick-solid line denotes the fitting formula given by Equation (13). Taken from [96].

It is well known that the overtone frequencies of torsional oscillations weakly depend on ℓ, unlike the fundamental oscillations [101]. As an example, in the left panel, we show the 1st overtones of the $\ell = 2$ (solid lines) and 10 (dashed lines) torsional oscillations as a function of ς for a neutron star models with $(M, R) = (1.4 M_\odot, 10 \text{ km})$, $(1.6 M_\odot, 12 \text{ km})$, and $(1.8 M_\odot, 14 \text{ km})$ with $N_s/N_d = 1$ in the phase of cylindrical nuclei. From this figure, one confirms that $_1 t_\ell$ weakly depends on ℓ, while one also finds that $_1 t_\ell$ strongly depends on the stellar models. So, hereafter, in this review, we focus only on $_n t_2$ to discuss the ς dependence of the overtones. In addition, in the right panel, we show the ς dependence of $_1 t_2$ for the $1.4 M_\odot$ neutron star models with different radii with $N_s/N_d = 1$ in the phase of cylindrical nuclei together with the 626.5 Hz QPO observed in SGR 1806-20. From this figure, one can observe that the optimal values of ς are 178.5, 149.7, and 107.1 MeV for $1.4 M_\odot$ neutron stars of $R = 10$, 12, and 14 km, respectively, if one identifies the 626.5 Hz QPO with the 1st overtone.
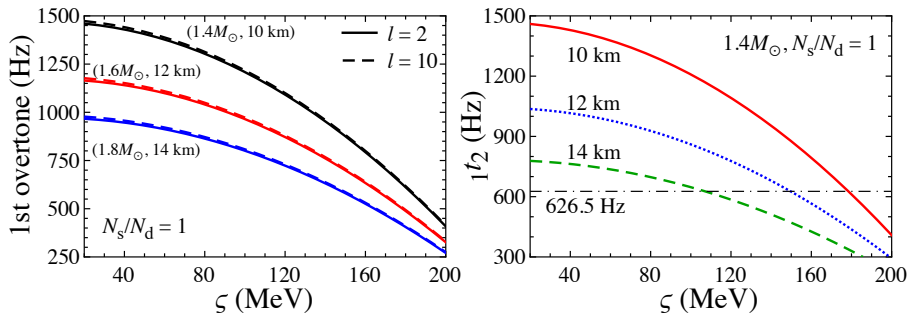

Figure 13. In the left panel, we show the 1st overtones of the $\ell = 2$ (solid lines) and 10 (dashed lines) torsional oscillations as a function of ς for a neutron star models with $(M, R) = (1.4 M_\odot, 10 \text{ km})$, $(1.6 M_\odot, 12 \text{ km})$, and $(1.8 M_\odot, 14 \text{ km})$ with $N_s/N_d = 1$ in the phase of cylindrical nuclei. In the right panel, the ς dependence of the 1st overtone of the $\ell = 2$ torsional oscillations for $1.4 M_\odot$ neutron star models with $R = 10$ km (solid line), 12 km (dotted line), and 14 km (dashed line) with $N_s/N_d = 1$ in the phase of cylindrical nuclei is compared to the 626.5 Hz QPO observed in SGR 1806-20 (dot-dashed line). Taken from [96].

In a similar way, one can obtain the optimal values of ς for various neutron star models. In the left panel of Figure 14, the resultant optimal values of ς are plotted for neutron star models with $1.4 \leq M/M_\odot \leq 1.8$ and $10 \text{ km} \leq R \leq 14 \text{ km}$ for $N_s/N_d = 1$ in the phase of cylindrical nuclei. One can observe that for each R, the optimal ς increases with M. This behavior comes from the fact that $\Delta R/R$

(or ΔR with fixed R) decreases with the compactness, M/R [81], which leads to the increases of $_1 t_2$ (through $_1 t_2 \sim v_s / \Delta R$) and that a optimal value of ς becomes larger.
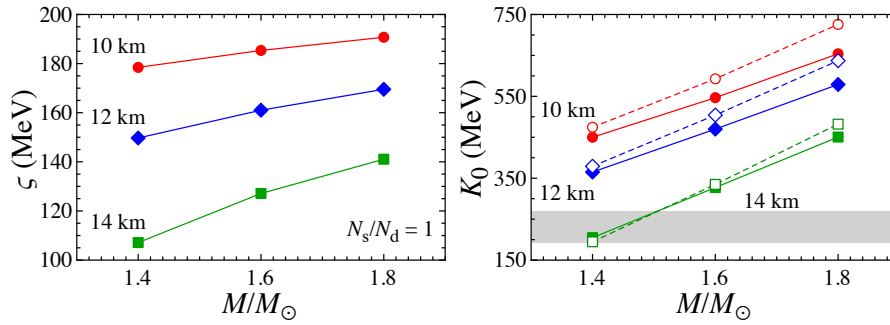

Figure 14. In the left panel, the optimal value of ς to identify the 626.5 Hz QPO observed in SGR 1806-20 with the 1st overtone of the $\ell = 2$ torsional oscillations are plotted for various neutron star models with $1.4 \le M/M_\odot \le 1.8$ and $10 \text{ km} \le R \le 14 \text{ km}$ for $N_s/N_d = 1$ in the phase of cylindrical nuclei. In the right panel, the constraint on K_0 obtained by combining the optimal values of ς shown in the left panel (and also those obtained with $N_s/N_d = 0$) and the optimal values of L shown in Figure 11 is plotted for each stellar model, where filled marks with solid lines (open marks with dashed lines) denote the results for $N_s/N_d = 1$ (0) in the phase of cylindrical nuclei. Meanwhile, the shaded region denotes the experimental constraint on K_0 obtained in [4], i.e., $K_0 = 230 \pm 40$ MeV. Taken from [96].

Furthermore, we also derive constraint on K_0 through the definition of ς given by Equation (12), i.e., $K_0 = (\varsigma^9/L^5)^{1/4}$, using the optimal values of ς for identifying the 626.5 Hz QPO with the 1st overtone frequency shown in the left panel of Figure 14 and the optimal values of L for identifying the low-lying QPO frequencies shown in Figure 11. In the right panel of Figure 14, such constraints on K_0 are plotted for various neutron star models, where the filled marks with solid lines denote the results for $N_s/N_d = 1$, while the open marks with dashed lines denote the results for $N_s/N_d = 0$. In the same panel, we also show the experimental constraint on K_0, i.e., $K_0 = 230 \pm 40$ MeV [4]. Adopting this constraint on K_0 as a typical one, although it may still be model dependent, e.g., [5], from the right panel of Figure 14 one can observe that the neutron star models with $M \simeq 1.4 - 1.5 M_\odot$ for $R = 14$ km and presumably $M \simeq 1.2 - 1.4 M_\odot$ for $R = 13$ km are favored by the QPOs observed in SGR 1806–20 up to 626.5 Hz (except for the 26 Hz QPO). That is, a central object in SGR 1806–20 would have a relatively low mass and large radius. We note in passing that a neutron star model with still lower mass and smaller radius than that mentioned above might be acceptable from the right panel of Figure 14, but one has to assume a larger value of L to construct such a stellar model, which would be presumably inconsistent with the systematic analysis of the mass-radius relation for low-mass neutron stars [34].

Finally, adopting the resultant constraint on the neutron star model of SGR 1806-20, i.e., $M \simeq 1.4 - 1.5 M_\odot$ for $R = 14$ km and $M \simeq 1.2 - 1.4 M_\odot$ for $R = 13$ km, the constraints on L shown in Figure 11 are dramatically improved. Namely, the optimal value of L should be $L \simeq 62 - 73$ MeV for $N_s/N_d = 1$ and $L \simeq 58 - 70$ MeV for $N_s/N_d = 0$ in the phase of cylindrical nuclei. Therefore, we obtain the constraint on L as $L \simeq 58 - 73$ independently of the uncertainty in N_s/N_d in the phase of cylindrical nuclei, which is consistent with the existing constraint on L, e.g., [3,7,9]. Using the correlation between L and S_0 (Equation (11)), one can estimate the corresponding value of S_0 as $S_0 \simeq 32.4 - 33.5$ MeV.

5.3. Torsional Oscillations Excited in the Cylindrical-Hole and Spherical-Hole Nuclei

Through Sections 5.1 and 5.2, we discussed that the QPO frequencies observed in SGR 1806-20 and SGR 1900+14 are well identified with the torsional oscillations excited in the phase of spherical and cylindrical nuclei. In particular, by identifying the 626.5 Hz QPO with the 1st overtone of the torsional

oscillations, we showed the possibility that a central object in SGR 1806-20 would be a neutron star with a relatively low mass and large radius, and derived the constraint on L more severe. However, still, we have a missing piece in the identification of the observed QPO frequencies, i.e., the 26 Hz QPO observed in SGR 1806-20. In this subsection, we discuss the possibility of identifying the 26 Hz QPO (and the QPOs additionally discovered in [58]) in SGR 1806-20 with the torsional oscillations excited in the phase of cylindrical-hole and spherical-hole nuclei, keeping the consistency with the identification discussed in Section 5.2.

To determine the frequencies of torsional oscillations excited in the phase of cylindrical-hole and spherical-hole nuclei, one has to know the value of $\mathcal{R}$ in Equation (8) in the phases of cylindrical-hole and spherical-hole nuclei, but it is still quite uncertain. So, here we simply consider the extreme cases, i.e., $\mathcal{R} = 1$ for maximum enthalpy and 0 for minimum enthalpy. In Figure 15, we show the fundamental frequencies of the $\ell = 2$ torsional oscillations excited in the phase of cylindrical-hole and spherical-hole nuclei for a neutron star model with $1.4 M_\odot$ and 12 km, using the EOSs with some parameter sets listed in Table 1 (see Ref. [69] for the concrete parameter sets adopted here), where the left and right panels correspond to the results with $\mathcal{R} = 1$ and 0 in the phase of cylindrical-hole and spherical-hole nuclei, respectively. From this future, we find that the fundamental frequencies excited in the phase of cylindrical-hole and spherical-hole nuclei weakly depend on K_0 and the dependence on L is well fitted with the functional form given by

$$_0 t_\ell = \tilde{c}_\ell^{(0)} + \tilde{c}_\ell^{(1)} \sqrt{L} + \tilde{c}_\ell^{(2)} L, \tag{14}$$

where $\tilde{c}_\ell^{(i)}$ for $i = 0, 1, 2$ are the adjustable parameters depending on M, R, and $\mathcal{R}$ in the phase of cylindrical-hole and spherical-hole nuclei [69]. Using this L dependence of $_0 t_\ell$ excited in the phase of cylindrical-hole and spherical-hole nuclei, we will see the correspondence of the observed QPOs.
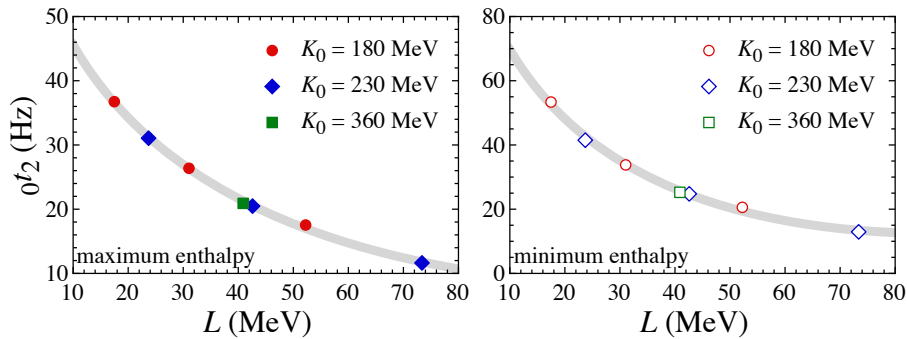

Figure 15. The fundamental frequencies of the $\ell = 2$ torsional oscillations excited in the phase of cylindrical-hole and spherical-hole nuclei for a neutron star model with $1.4 M_\odot$ and 12 km. The thick-solid line corresponds to the fitting formula given by Equation (14). The left and right panels respectively correspond to the results with $\mathcal{R} = 1$ (maximum enthalpy) and $\mathcal{R} = 0$ (minimum enthalpy). Taken from [69].

In the left panel of Figure 16, we show the identification of the low-lying QPOs observed in SGR 1806-20 with the fundamental frequencies of torsional oscillations excited in the phase of spherical and cylindrical nuclei and the phase of cylindrical-hole and spherical-hole nuclei for a neutron star model with $1.3 M_\odot$ and 13 km. As shown in the left panel of Figure 10, the 18, 29, 57, 92.5 Hz QPOs can be identified with the fundamental frequencies of the $\ell = 2, 3, 6, 10$ torsional oscillations excited in the phase of spherical and cylindrical nuclei. With this correspondence, we find the optimal values of L as $L \simeq 70.8$ MeV for $N_s/N_d = 1$ and $L \simeq 67.5$ MeV for $N_s/N_d = 0$ in the phase of cylindrical nuclei. We note that in Figure 16 the solid lines denote the fundamental frequencies of torsional oscillations excited in the phase of spherical and cylindrical nuclei with $N_s/N_d = 1$ in the phase of cylindrical nuclei. On the other hand, we also show the fundamental frequencies of $\ell = 2, 3, 4$ torsional oscillations

excited in the phase of cylindrical-hole and spherical-hole nuclei by the shaded regions, assuming that $0 \leq \mathcal{R} \leq 1$. From this figure, one can observe that the 26 Hz QPO, which cannot be identified with the torsional oscillations in the phase of spherical and cylindrical nuclei, can be identified with the $\ell = 4$ fundamental torsional oscillations excited in the phase of cylindrical-hole and spherical-hole nuclei consistently with the optimal value of L given by the identification of the other QPOs with the torsional oscillations in the phase of spherical and cylindrical nuclei.
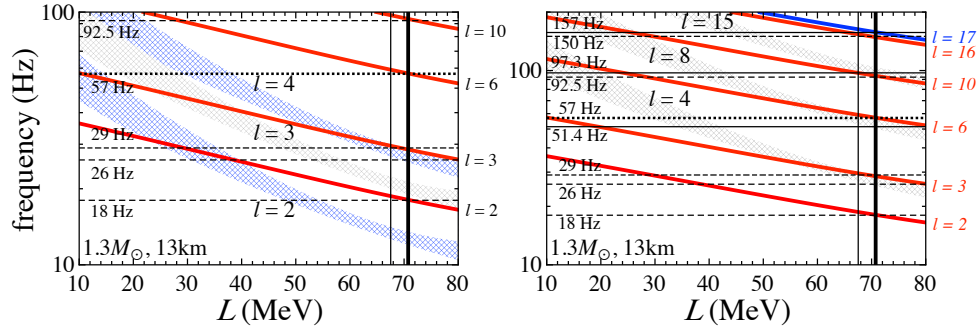

Figure 16. The correspondence of the QPO frequencies observed in SGR 1806-20 and the fundamental frequencies of torsional oscillations with various values of ℓ excited in the phase of spherical and cylindrical nuclei with $N_s/N_d = 1$ in the cylindrical nuclei (solid lines) and the phase of cylindrical-hole and spherical-hole nuclei for $0 \leq \mathcal{R} \leq 1$ (shaded regions) for a neutron star model with $1.3M_\odot$ and 13 km. We focus on only the low-lying QPOs in the left panel, while in the right panel we also consider the QPOs additionally discovered in [58] together with the QPOs considered in the left panel. The vertical lines denote the optimal values of L to identify the low-lying QPO frequencies observed in SGR 1806-20 except for the 26 Hz QPO with the torsional oscillations excited in the phase of spherical and cylindrical nuclei discussed in Section 5.2, where the thick line ($L \simeq 70.8$ MeV) and thin line ($L \simeq 67.5$ MeV) respectively correspond to the optimal values of L with $N_s/N_d = 1$ and 0 in the phase of cylindrical nuclei. Taken from [69].

In addition, using this double layer model (lasagna sandwich model), we find that one can identify the QPOs originally discovered in SGR 1806-20 together with the QPOs additionally discovered by a Bayesian procedure, e.g., 51.4, 97.3, and 157 Hz QPOs [58], as shown in the right panel of Figure 16. That is, as shown in left panel of Figure 10, the 18, 29, 57, 92.5, and 150 Hz QPOs can be identified with the fundamental frequencies of the $\ell = 2, 3, 6, 10$, and 16 torsional oscillations excited in the phase of spherical and cylindrical nuclei. In a similar way, the 157 Hz QPO can be identified with the $\ell = 17$ fundamental torsional oscillations in the phase of spherical and cylindrical nuclei, while the 26, 51.4, and 97.3 Hz QPOs are the $\ell = 4, 8$, and 15 fundamental torsional oscillations in the phase of cylindrical-hole and spherical-hole nuclei.

5.4. Constraint on a Neutron Star Model for GRB 200415A

So far, we have considered the correspondence between the crustal torsional oscillations and the QPO frequencies observed in giant flares. In addition to these observations, another magnetar flare, GRB 200415A, was also detected in the direction of the NGC253 galaxy, where several high-frequency QPOs with varying significance were found at 836, 1444, 2132, and 4250 Hz [59]. We note that only high-frequency QPOs have been detected from this event due to the short duration of the observation interval. So, considering the dynamical time of neutron stars, it may be possible to identify these observed QPOs with neutron star oscillations other than the torsional oscillations, such as the fundamental (f-), gravity (g_i-), or shear (s_i-) modes (e.g., see Figure 25). Nevertheless, since these QPOs come from the magnetar flare, here we consider the identification with the crustal torsional oscillations, which is the same framework as discussed in the case of the QPOs observed in giant flares (Sections 5.1–5.3).

Since the observed QPOs are too high to identify the fundamental torsional oscillations, we consider identifying them with the overtones of torsional oscillations, as in Section 5.2. Using the fitting of the overtone frequencies given by Equation (13), we plot the ς dependence of $_nt_2$ in the left panel of Figure 17 for a neutron star model with $1.6M_\odot$ and 12 km with $N_s/N_d = 0$ in the phase of cylindrical nuclei, where the horizontal shaded regions denote the QPOs observed in GRB 200415A. We note that the overtone frequencies weakly depend on the ratio of N_s/N_d in the phase of cylindrical nuclei [75], in this subsection, we only consider the case with $N_s/N_d = 0$ in the phase of cylindrical nuclei. From this figure, one can observe that the four QPOs can be identified well with the 1st, 2nd, 4th, and 10th overtones of torsional oscillations, which tells us the optimal value of ς is 121.7 MeV.

In a similar way, one can determine the optimal values of ς for various neutron star models. In practice, the optimal values of ς determined with the same combination of the overtones as shown in the left panel of Figure 17 are plotted in the right panel of Figure 17. In particular, the neutron star model considered in the left panel is indicated with the arrow. Meanwhile, the value of ς is also estimated with the fiducial value of L and K_0, i.e., $\varsigma = 83.5 - 135.1$ MeV with $L = 60 \pm 20$ MeV and $K_0 = 240 \pm 20$ MeV [2], or with the optimal value of L obtained in Section 5.2 to identify the QPO frequencies observed in the giant flares with the torsional oscillations, such as $L = 58 - 73$ MeV, with the fiducial value of K_0, i.e., $\varsigma_{QPO} = 104.9 - 128.4$ MeV. These estimations of ς are also shown in the right panel of Figure 17 with the shaded region and the enclosed region with the dashed lines. That is, considering these estimations, for example the stellar model with $1.5M_\odot$ and 11 km can be excluded. In consequence, we can get the constraint on the neutron star mass and radius as shown in the left panel of Figure 18, where the shaded region corresponds to the results with $\varsigma = 83.5 - 135.1$ MeV, while the bound region by solid lines is those with $\varsigma_{QPO} = 104.9 - 128.4$ MeV.
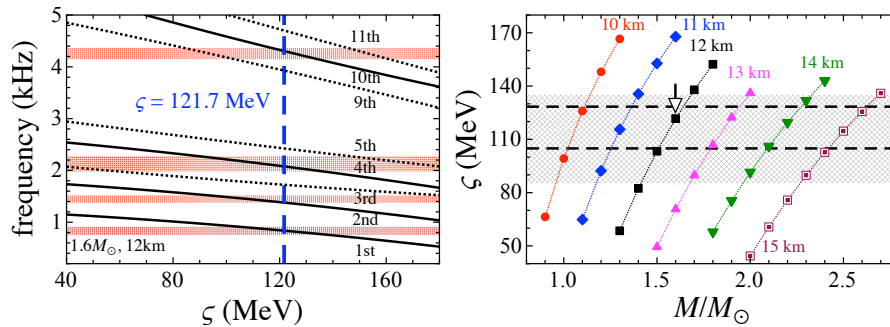

Figure 17. In the left panel, we show the identification of four QPO frequencies observed in GRB 200415A [59] (shaded horizontal regions) with several overtones of torsional oscillations excited in the phase of spherical and cylindrical nuclei for a neutron star model with $1.6M_\odot$ and 12 km with $N_s/N_d = 0$ in the phase of cylindrical nuclei, where $\varsigma = 121.7$ is the optimal value with this correspondence. In the right panel, we show the optimal values of ς to identify the four QPOs in GRB 200415A with the same combinations of overtones as in the left panel for various neutron star models. The shaded region is the range of $\varsigma = 85.3 - 135.1$ MeV estimated with the fiducial value of $L = 60 \pm 20$ MeV and $K_0 = 240 \pm 20$ MeV, while the region in the dashed lines is the range of $\varsigma_{QPO} = 104.9 - 128.4$ MeV with the optimal values of L discussed in Section 5.2, i.e., $L = 58 - 73$ MeV, together with $K_0 = 240 \pm 20$ MeV. The arrow in the right panel indicates the neutron star model considered in the left panel. Taken from [75].
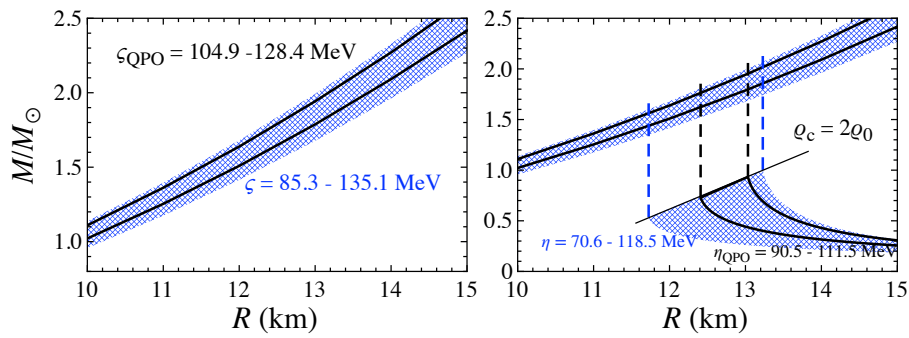
Figure 18. In the left panel, the constraint on the neutron star mass and radius for GRB 200415A obtained from the optimal values of ς to identify the high-frequency QPOs with 1st, 2nd, 4th, and 10th overtones of torsional oscillations, adopting the range of $\varsigma = 85.3 - 135.1$ MeV estimated with the fiducial value of L and K_0 (shaded region) or $\varsigma_{QPO} = 104.9 - 128.4$ MeV with the optimal value of L to identify the magnetar QPOs (bound by solid lines). In the right panel, we show the constraint on the neutron star mass and radius obtained from the QPOs in GRB 200415A (the same as the left panel) together with those estimated with the mass formula for a low-mass neutron star as a function of $\eta = (K_0 L^2)^{1/3}$ derived in [34] (the right-bottom region), assuming that the central density of neutron stars should be less than twice the nuclear saturation density. Taken from [75].

One may make the constraint on the mass and radius of the neutron star model for GRB 200415A more severe, if one knows the EOSs (or mass-radius relations) corresponding to the estimations of ς. For this purpose, the mass formula for a low-mass neutron star [34] must be crucial. The low-mass neutron star structures may strongly depend on the nuclear saturation parameters, because the central density for such an object is very low. In fact, the mass and gravitational redshift, z, defined by $z = 1/\sqrt{1 - 2M/R} - 1$ can be well expressed as a function of the stellar central density and a new parameter given by

$$\eta \equiv (K_0 L^2)^{1/3}, \tag{15}$$

such as

$$M/M_\odot = 0.371 - 0.820 u_c + 0.279 u_c^2 - (0.593 - 1.25 u_c + 0.235 u_c^2)\eta_{100}, \tag{16}$$

$$z = 0.00859 - 0.0619 u_c + 0.0255 u_c^2 - (0.0429 - 0.108 u_c + 0.0120 u_c^2)\eta_{100}, \tag{17}$$

where u_c is the central density of the neutron star normalized by the saturation density and η_{100} is the value of η normalized by 100 MeV [34]. We note that these empirical formulae are valid in the range of $0.9 \lesssim u_c \leq 2.0$. Since z is a combination of M and R, one can plot the mass and radius relation once one selects the value of η.

The values of ς and ς_{QPO}, which are adopted to make a constraint on the mass and radius of the neutron star shown in the left panel of Figure 18, are respectively given by $L = 60 \pm 20$ MeV and $L = 58 - 73$ with $K_0 = 240 \pm 20$ MeV, which correspond to the value of η as $\eta = 70.6 - 118.5$ MeV and $\eta_{QPO} = 90.5 - 111.5$ MeV, respectively. Using this range of η, one can estimate the stellar mass and radius, whose central density is less than twice the saturation density, as the right-bottom regions in the right panel of Figure 18. Furthermore, assuming that the radius of the neutron star whose central density is larger than twice the saturation density would be almost constant as shown with the dashed lines corresponding to $R = 11.73, 12.41, 13.03$, and 13.23 km for $\eta = 70.6, 90.5, 111.5$, and 118.5 MeV, we can get the overlap region with the constraint on the neutron star mass and radius to identify the QPOs with the overtones of torsional oscillations shown in the left panel of Figure 18. In such a way, we can get the neutron star mass and radius constraint for GRB 200415A. The resultant mass and radius constraint is shown in Figure 19 with a double-parallelogram, together with the other constraints obtained from the astronomical observations and experimental constraints.
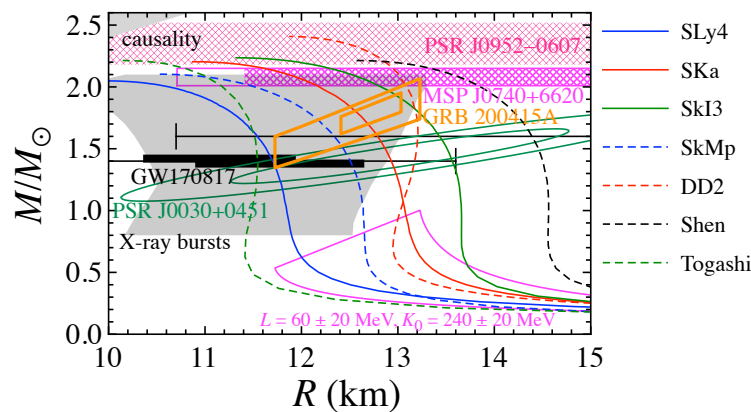
Figure 19. Mass and radius of GRB 200415A constrained by identifying the observed high-frequency QPOs with the overtones of crustal torsional oscillations (double-parallelogram), adopting the fiducial values of L and K_0 (or the optimal value of L to identify the magnetar QPOs). For reference, the other constraints obtained from the astronomical observations and experimental restrictions are also shown. For astronomical observations, as well as those shown in Figure 1, we plot the constraints of the $1.6M_\odot$ neutron star radius, i.e., $R_{1.6} \gtrsim 10.7$ km [105], the $1.4M_\odot$ neutron star radius, i.e., $R_{1.4} = 11.0^{+0.9}_{-0.6}$ km [106] or $R_{1.4} = 11.75^{+0.86}_{-0.81}$ km [107] obtained from the GW170817; and the massive neutron star mass of PSR J0952-0607, i.e., $M = 2.35 \pm 0.17M_\odot$ [108]. Taken from [75].

Finally, we comment on the alternative identification of the QPOs observed in GRB 200415A with the overtones of torsional oscillations. To obtain the neutron star mass and radius constraint shown in Figure 19, we identify the lowest QPO observed in GRB 200415A, i.e., 835.9 Hz QPO, with the 1st overtone of the torsional oscillations, but it may be possible to identify it with the 2nd overtone. In the left panel of Figure 20, we compare the lowest QPO observed in GRB 200415A with the 1st (dotted line) and 2nd (solid line) overtones for a neutron star model with $1.4M_\odot$ and 14 km. In this figure, we also show the range of ς with the fiducial value of L and K_0 (shaded region) and that with the optimal value of L to identify the QPOs observed in the giant flares (the region between the vertical dashed lines). From this figure, one can find that the lowest QPO observed in GRB 200415A cannot be identified with the 2nd overtone at least with this stellar model, consistently with the region of ς estimated with the fiducial value of saturation parameters. In practice, one can identify the four QPOs observed in GRB 200415A with the 2nd, 5th, 8th, and 16th overtones, if $\varsigma \simeq 142$ MeV, as shown in the right panel of Figure 20. Still, anyway, it is inconsistent with the range of ς with the fiducial value of saturation parameters.
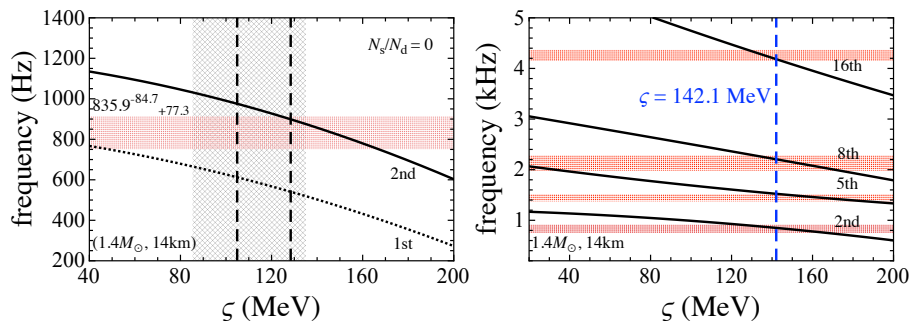
Figure 20. An alternative possibility to identify the observed QPOs in GRB 200415A with the overtones of torsional oscillations, i.e., the lowest QPO frequency is identified with the 2nd overtone instead of the 1st overtone. In the left panel, the lowest QPO frequency (shaded horizontal region) is compared with the 1st (dotted line) and 2nd (solid line) overtones as a function of ς for a neutron star model with $1.4M_\odot$ and 12 km. The vertical shaded region corresponds to $\varsigma = 85.3 - 135.1$ MeV with fiducial values of L and K_0, while the region between the vertical dashed lines is $\varsigma_{QPO} = 104.9 - 128.4$ MeV. In the right panel, the four observed QPOs are identified with the 2nd, 5th, 8th, and 16th overtones for a neutron star model with $1.4M_\odot$ and 14 km. The vertical dashed line denotes the optimal value of ς with this correspondence. Taken from [75].

6. Shear and Interface Oscillations

Owing to the presence of the crust elasticity, the shear (s-) and interface (i-) modes are also excited as well as the torsional oscillations. To see the behavior of the s- and i-mode frequencies, again we consider the stellar model with the pasta phases, where the elasticity in the phase composed of slablike nuclei is assumed to be zero. In the same as in the torsional oscillations, one has to consider the effect of the neutron superfluidity, i.e., N_s/N_d to estimate the value of N_s in Equation (7) and $\mathcal{R}$ in Equation (8), but for simplicity we consider only the situation of the maximum enthalpy here, i.e., all the dripped neutron comove with the protons.

In this review, we simply adopt the Cowling approximation to examine the s- and i-mode oscillations. Therefore, the perturbation equations for the s- and i-modes are derived from the linearized energy-momentum conservation laws, which are completely the same as those for the f-, p_i-, and g_i-modes if one neglects the elasticity. One can find the concrete perturbation equations in [82,109], even though they are not shown explicitly here. We note that the perturbation equations without the Cowling approximation are also found in [42], which can be obtained from the linearized Einstein equations. As the boundary conditions, one should impose the regularity condition at the center and the condition that the Lagrangian perturbation of pressure should be zero at the stellar surface. In addition, at the interface where the elasticity discontinuously becomes zero, one has to impose the junction conditions, such as the continuity of the radial displacement, the radial and transverse tractions, and Lagrangian perturbation of pressure [109,110]. In practice, with our stellar models, one has to impose the junction conditions at the four interfaces, i.e., between the fluid core and the phase of spherical-hole nuclei, between the phase of cylindrical-hole nuclei and the phase of slablike nuclei, between the phase of slablike nuclei and the phase of cylindrical nuclei, and between the surface of the outer crust and envelope.

The transition density at these interfaces becomes crucial for the s- and i-mode oscillations. The transition density where the nuclear shape would be changed is determined from the EOS, depending on the saturation parameters, e.g., [78–80]. On the other hand, the transition density at the outer crust surface is more or less complicated. This is because the density to determine such properties is too low to neglect the thermal effect, even though the thermal effect on the neutron star structure is negligible when the density is very high [111]. In this review, we simply consider that the transition density at the surface of the outer crust is 10^{10} g/cm^3. In addition, we set the surface density, ρ_s, being 10^6 g/cm^3.

In Figure 21, as an example, we show the radial profile of the amplitude of the Lagrangian displacement for the i_i-modes ($i = 1 - 4$) in the radial (W) and angular directions (V) for a stellar model with $1.44 M_\odot$ and 10.2 km constructed with the EOS with $K_0 = 230$ MeV and $L = 42.6$ MeV. The classification of i-mode is not uniquely fixed, but here we identify that the i_2-mode is mainly excited at the interface between the crust surface and envelope; the i_1-mode is excited at the interface between the crust surface and envelope and at the interface between the phase of slablike nuclei and the phase of cylindrical nuclei; the i_3- and i_4-modes are mainly excited at the interface associated with the cylindrical-hole and spherical-hole nuclei. Since the i-modes are eigenmodes excited due to the existence of the interface where the elasticity discontinuously becomes zero [113], the number of the excited i-modes is generally equivalent to the number of the interface [82,112]. With our classification, the order of the i-modes generally becomes i_4-, i_2-, i_1-, and i_3-mode from the lowest to highest, and typically the frequencies are less than ~ 100 Hz. Moreover, in Figure 22, we show how i-mode frequencies depend on the surface density, ρ_s, by fixing the other transition density. From this figure, one can observe the i-mode frequencies hardly depend on ρ_s.
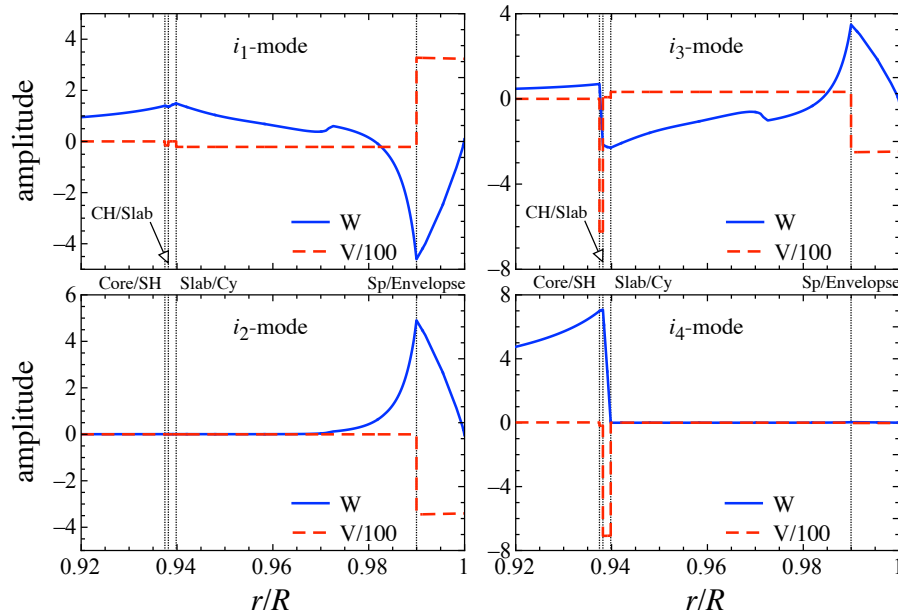

Figure 21. The radial profile of the amplitude of the Lagrangian displacement for the i_i-modes in the radial (W) and angular direction (V) for a stellar model with $1.44 M_\odot$ and 10.2 km constructed with the EOS with $K_0 = 230$ MeV and $L = 42.6$ MeV. The vertical dotted lines from left to right denote the interface between the fluid core and the phase of spherical-hole nuclei, the interface between the phase of cylindrical-hole and the phase of slablike nuclei, the interface between the phase of slablike nuclei and the phase of cylindrical nuclei, and the interface between the surface of crust and envelope. Taken from [112].

On the other hand, in Figure 23, we show the radial profile of the amplitude of the Lagrangian displacement for the s_1- and s_2-modes in the radial (W) and angular directions (V) for a neutron star model with $1.4 M_\odot$ and 12.4 km constructed with the EOS with $K_0 = 230$ MeV and $L = 73.4$ MeV. Unlike the i-modes, there are an infinite number of the s-modes. As shown in Figure 23, the s-modes are excited almost only inside the elastic region. Thus, in principle, one may find the s-modes excited inside the phase of cylindrical-hole and spherical-hole nuclei. Even so, we could not find them in the frequency range of less than a few kHz. This situation could be understood as follows. Focusing on the angular displacement, V, in Figure 23, one may see that the wavelength of the s_i-mode, λ_i, is roughly estimated as

$$\lambda_i \simeq 2\Delta R / i, \tag{18}$$

where ΔR denotes the thickness of the elastic region where the s-mode is confined. Meanwhile, the s_i-mode frequency may be estimated as

$$f_{s_i} \simeq v_s / \lambda_i, \tag{19}$$

using the shear velocity, v_s, [42]. With this simple estimation, one can expect that, even if the s-modes are excited inside the phase of cylindrical-hole and spherical-hole nuclei, their frequencies must become much higher than those excited in the phase of spherical and cylindrical nuclei. Namely, ΔR for the phase of cylindrical-hole and spherical-hole nuclei, ΔR_{CHSH}, is much thinner than ΔR for the phase of spherical and cylindrical nuclei, ΔR_{SpCy}, i.e., $\Delta R_{CHSH}/\Delta R_{SpCy} \sim 1/100$, which leads to the estimation that the s-mode frequencies excited in the phase of cylindrical-hole and spherical-hole nuclei must be ~ 100 times higher than those excited in the phase of spherical and cylindrical nuclei.
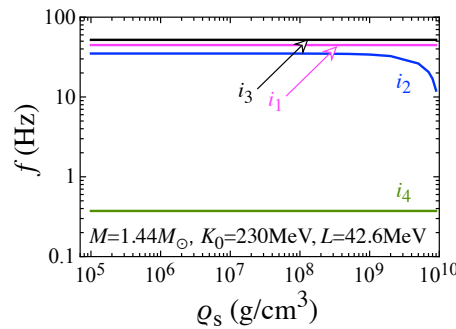

Figure 22. Dependence of the i-mode frequencies on the surface density, ρ_s, for a neutron star model with $M = 1.44 M_\odot$ constructed with $K_0 = 230$ MeV and $L = 42.6$ MeV. The other transition density between the phases with and without elasticity is fixed. Taken from [112].
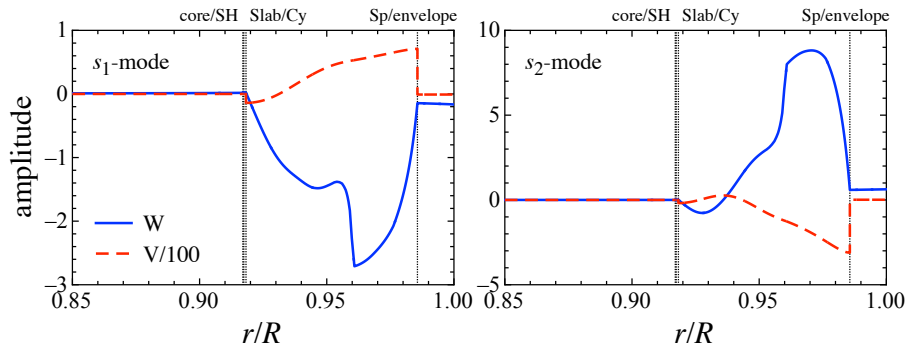

Figure 23. The radial profile of the amplitude of the Lagrangian displacement for the s_1- and s_2-modes in the radial (W) and angular direction (V) for a neutron star model with $1.4 M_\odot$ and 12.4 km constructed with the EOS with $K_0 = 230$ MeV and $L = 73.4$ MeV. Taken from [82].

Since the crust thickness, ΔR, also depends on the stellar compactness [77,81], to see the dependence of the s- and i-mode frequencies on the neuron star properties, we consider not only the neutron star models constructed with the original OI-EOSs but also those constructed with the EOS, which is constructed in such a way that the OI-EOS for a lower density region ($\varepsilon \leq \varepsilon_t$) is connected to a one-parameter EOS given by

$$p = \alpha(\varepsilon - \varepsilon_t) + p_t, \tag{20}$$

for a higher density region ($\varepsilon \geq \varepsilon_t$), where we especially adopt that ε_t is equivalent to twice the saturation density [114]. In the one parameter EOS, p_t is given from the OI-EOS at $\varepsilon = \varepsilon_t$ and α is related to the sound velocity, c_s, as $c_s^2 = \alpha$. Thus, α is a kind of indicator for expressing the stiffness of the core (or higher density) region. In this review, we focus on $1/3 \leq \alpha \leq 1$.

Through a systematical study, we find empirical relations for the i_i-mode frequency, f_{i_i}, and the s_i-mode frequency, f_{s_i}. That is, $f_{i_i} M$ and $f_{s_i} R$ can be expressed as a function of the stellar compactness, x, given by $x \equiv M_{1.4}/R_{12}$ with $M_{1.4} = M/1.4 M_\odot$ and $R_{12} = R/12 \text{km}$, almost independently of the stiffness of the core region, i.e., the value of α, such as

$$f_{i_i} M \ (\text{kHz}/M_\odot) = a_{0i} + a_{1i}x + a_{2i}x^2, \tag{21}$$

$$f_{s_i} R \ (\text{kHz km}) = b_{0i} + b_{1i}x, \tag{22}$$

where a_{0i}, a_{1i}, a_{2i}, b_{0i}, and b_{1i} are the adjusted coefficients depending on the crust properties [82]. As an example, in Figure 24, we show the results for the i_1-mode (left panel) and the s_1-mode (right panel), where the solid lines denote the fitting given by Eqs. (21) and (22). Thus, once one simultaneously observes the shear and interface mode frequencies from a neutron star, one might extract the neutron star mass and radius via the empirical relations given by Eqs. (21) and (22) with the help of the constraint on the crust stiffness obtained from terrestrial experiments. Furthermore, the coefficients in Eqs. (21) and (22) can be well fitted as a function of a suitable combination of K_0 and L [82]. Namele, $f_{i_i} M$ and $f_{s_i} R$ can be expressed as a function of M/R and a combination of K_0 and L. In practice, the s-mode frequency for a canonical neutron star can be estimated within $\sim 1\%$ accuracy.
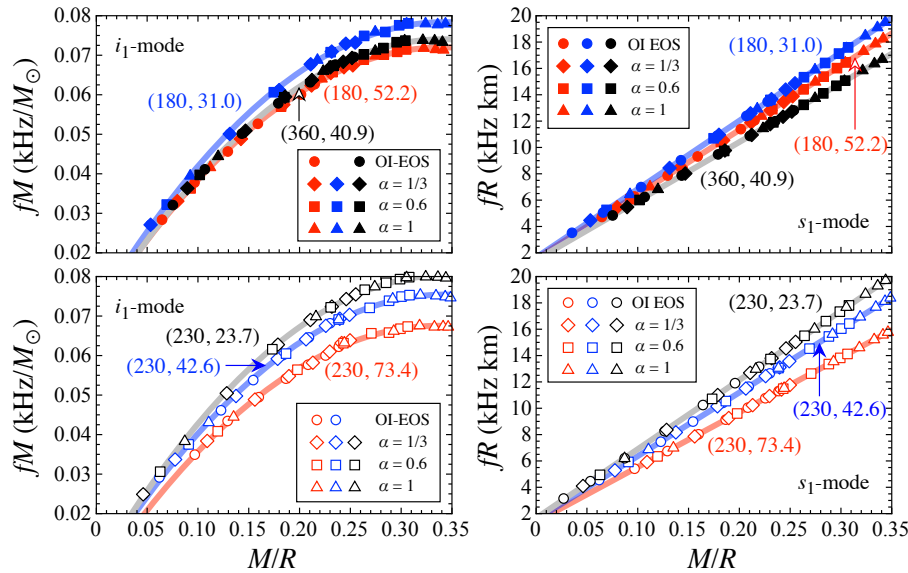

Figure 24. For various neutron star models, $f_{i_1} M$ and $f_{s_1} R$ are respectively plotted as a function of M/R in the left and right panels, where the circles, diamonds, squares, and triangles denote the results for stellar models constructed with the original OI-EOS, OI-EOS connected to the EOS with $\alpha = 1/3$, 0.6, and 1, respectively. The solid lines denote the fitting by Eqs. (21) in the left panel and (22) in the right panel, while the values of the EOS parameters (K_0, L) are also shown on each line. Taken from [112].

At the end, we consider the possibility of applying the s-mode frequency for identifying the QPO observations. As discussed in Section 5.4, one can identify the high-frequency QPOs observed in GRB 200415A with the overtones of crustal torsional oscillations. Since only high-frequency QPOs have been observed in this event, one may identify them with the other neutron star oscillations. In practice, as shown in Figure 25 where the f- and s_i-mode frequencies for the stellar models with $(K_0, L) = (230, 42.6)$ are shown as a function of the stellar compactness, together with the QPO frequencies observed in GRB 200415A, one can identify them with the s-modes. Namely, the observed QPOs are identified with the s_1-, s_2-, s_4-, and s_8-mode frequencies if $M/R \simeq 0.183$ for $\alpha = 1/3$ (left panel) or $M/R \simeq 0.195$ for $\alpha = 0.6$ (right panel). One could discuss the constraint on the saturation

parameters through the identification of the QPOs with the torsional oscillations in Sec.5, because the torsional oscillations are confined inside the elastic region. On the other hand, since the s-mode oscillations depend on not only the crust region (elastic region) but also the (fluid) core region, it may be more difficult to discuss the crust properties via the identification of QPOs with the s-modes. Anyway, to get a severe constraint on the neutron star properties or to validate a theoretical model, we have to wait for the next signals from a neutron star.
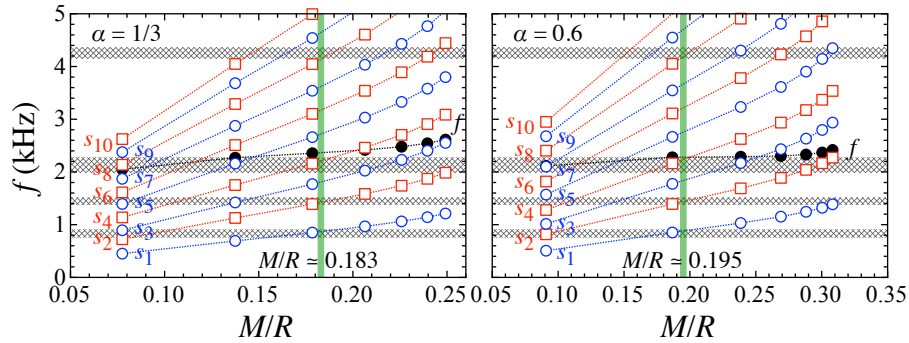

Figure 25. The f- and s_i-mode ($i = 1 - 10$) frequencies are shown as a function of M/R for neutron star models constructed with the EOS parameter of $(K_0, L) = (230, 42.6)$, where the left and right panels correspond to the results for $\alpha = 1/3$ and 0.6, respectively. The horizontal shaded regions denote the QPO frequencies observed in GRB 200415A [59]. The vertical lines denote the optimal value of M/R to identify the four observed QPOs with the s_i-modes, i.e., $M/R \simeq 0.183$ for $\alpha = 1/3$ and $M/R \simeq 0.195$ for $\alpha = 0.6$. Taken from [112].

7. Discussion and Conclusions

In this review, we discussed the neutron star oscillations excited by the crust elasticity, such as the torsional, interface, and shear oscillations, adopting the Cowling approximation. Since the torsional oscillations are axial-type oscillations, one can fully discuss them even with the Cowling approximation. On the other hand, since the interface and shear oscillations are polar-type oscillations, one can qualitatively discuss them with the Cowling approximation but one may have to check the accuracy of the interface and shear mode frequencies by comparing them to those taken into account metric perturbations. In any case, through the identification of the QPOs observed in the magnetar flares with the torsional oscillations, we successfully obtain the constraint on the nuclear saturation parameters, especially the density dependence of the nuclear symmetry energy, L. On the other hand, via systematical study of the interface and shear oscillations, we find empirical relations almost independent of the stiffness of the core region.

To determine these frequencies, the effect of the superfluidity is important input physics as well as the shear modulus. To deal with the superfluidity, we introduce the parameter, such as N_s/N_d or $\mathcal{R}$, which is still quite uncertain. In addition, the understanding of the shear modulus inside the pasta phases may still be poor, where one has room for improvement. One may have to improve these properties to consider a more realistic situation.

Moreover, in this review, we consider only the oscillations excited due to the crust elasticity. Meanwhile, the existence of quark matter inside the neutron star is theoretically suggested. In such a situation, the hadronic matter would transition into quark matter, and the mixed phase may appear at the transition region, where the structure becomes similar to the pasta structure in the crust [115,116]. So, such a mixed phase behaves as a liquid crystal, i.e., the elasticity becomes non-zero. That is, if such a phase exists, one can expect that the torsional oscillations and/or shear and interface oscillations are excited in the hadron-quark mixed phase [117,118]. Through the observations of these oscillation modes, one may probe the properties of quark matter.

Institutional Review Board Statement: Not applicable.

Informed Consent Statement: Not applicable.

Data Availability Statement: Dataset available on request from the authors.

Conflicts of Interest: The authors declare no conflicts of interest. The funders had no role in the design of the study; in the collection, analyses, or interpretation of data; in the writing of the manuscript; or in the decision to publish the results.

Abbreviations

The following abbreviations are used in this manuscript:

QPOs   Quasi-periodic oscillations
SGR   Soft-gamma repeater
EOSs   Equations of state
TOV   Tolman-Oppenheimer-Volkoff

References

1. Shapiro, S. L.; Teukolsky, S. A. *Black Holes, White Dwarfs, and Neutron Stars: The Physics of Compact Objects*, Wiley-Interscience, New York, 1983.
2. Shlomo, S.; Kolomietz, V. M.; Colò, G. Deducing the nuclear-matter incompressibility coefficient from data on isoscalar compression modes. *Eur. Phys. J. A* **2006** *30*, 23.
3. Tsang, M. B. et. al. Constraints on the symmetry energy and neutron skins from experiments and theory. *Phys. Rev. C* **2012** *86*, 015803.
4. Khan, E.; Margueron, J. Determination of the density dependence of the nuclear incompressibility. *Phys. Rev. C* **2013** *88*, 034319.
5. Stone, J. R.; Stone, N. J.; Moszkowski, S. A. Incompressibility in finite nuclei and nuclear matter. *Phys. Rev. C* **2014** *89*, 044316.
6. Viñas, X.; Centelles, M.; Roca-Maza, X.; Warda, M. Density dependence of the symmetry energy from neutron skin thickness in finite nuclei. *Eur. Phys. J. A* **2014** *50*, 27.
7. Newton, W. G.; Hooker, J.; Gearheart, M.; Murphy, K.; Wen, D. H.; Fattoyev, F. J.; Li, B. A. Constraints on the symmetry energy from observational probes of the neutron star crust. *Eur. Phys. J. A* **2014** *50*, 41.
8. Oertel, M.; Hempel, M.; T. Klähn, T.; Typel, S. Equations of state for supernovae and compact stars. *Rev. Mod. Phys.* **2017** *89*, 015007.
9. Li, B. A.; Krastev, P. G.; Wen, D. H.; Zhang, N. B. Towards understanding astrophysical effects of nuclear symmetry energy. *Eur. Phys. J. A* **2019** *55*, 117.
10. Demorest, P.; Pennucci, T.; Ransom, S.; Roberts, M.; Hessels, J. A two-solar-mass neutron star measured using Shapiro delay. *Nature (London)* **2010**, *467*, 1081.
11. Antoniadis, J. et al. A Massive Pulsar in a Compact Relativistic Binary. *Science* **2013** *340*, 6131.
12. Cromartie, H. T. et al. Relativistic Shapiro delay measurements of an extremely massive millisecond pulsar. *Nat. Astron.* **2020** *4*, 72.
13. Fonseca, E. et al. Refined Mass and Geometric Measurements of the High-mass PSR J0740+6620. *Astrophys. J.* **2021** *915*, L12.
14. Abbott, B. P. et al. (The LIGO Scientific Collaboration and the Virgo Collaboration). GW170817: Observation of Gravitational Waves from a Binary Neutron Star Inspiral. *Phys. Rev. Lett.* **2017** *119*, 161101.
15. Annala, E.; Gorda, T.; Kurkela, A.; Vuorinen, A. Gravitational-Wave Constraints on the Neutron-Star-Matter Equation of State. *Phys. Rev. Lett.* **2018** *120*, 172703.
16. Pechenick, K. R.; Ftaclas, C.; Cohen, J. M. Hot spots on neutron stars - The near-field gravitational lens. *Astrophys. J.* **1983** *274*, 846.

17. Leahy, D. A.; Li, L. Including the effect of gravitational light bending in X-ray profile modelling. *Mon. Not. R. Astron. Soc.* **1995** *277*, 1177.

18. Poutanen, J.; Gierlinski, M. On the nature of the X-ray emission from the accreting millisecond pulsar SAX J1808.4-3658. *Mon. Not. R. Astron. Soc.* **2003** *343*, 1301.

19. Psaltis, D.; Özel, F. Pulse Profiles from Spinning Neutron Stars in the Hartle-Thorne Approximation. *Astrophys. J.* **2014** *792*, 87.

20. Sotani, H.; Miyamoto, U. Systematical study of pulsar light curves with special relativistic effects. *Phys. Rev. D* **2018** *98* 103019.

21. Sotani, H. Light curves from highly compact neutron stars with spot size effect. *Phys. Rev. D* **2020** *101*, 063013.

22. Riley, T. E. et al. A NICER View of PSR J0030+0451: Millisecond Pulsar Parameter Estimation. *Astrophys. J.* **2019** *887*, L21.

23. Miller, M. C. et al. PSR J0030+0451 Mass and Radius from NICER Data and Implications for the Properties of Neutron Star Matter. *Astrophys. J.* **2019** *887*, L24.

24. Riley, T. E. et al. A NICER View of the Massive Pulsar PSR J0740+6620 Informed by Radio Timing and XMM-Newton Spectroscopy. *Astrophys. J.* **2021** *918*, L27.

25. Miller, M. C. et al. The Radius of PSR J0740+6620 from NICER and XMM-Newton Data. *Astrophys. J.* **2021** *918*, L28.

26. Sotani, H.; Nishimura, N.; Naito, T. New constraints on the neutron-star mass and radius relation from terrestrial nuclear experiments. *Prog. Theor. Exp. Phys.* **2022**, *2022*, 041D01.

27. Sotani, H.; Ota, S. Neutron star mass formula with nuclear saturation parameters for asymmetric nuclear matter. *Phys. Rev. D* **2022**, *106*, 103005.

28. Sotani, H.; Naito, T. Empirical neutron star mass formula based on experimental observables. *Phys. Rev. C* **2023**, *107*, 035802.

29. Steiner, A. W.; Lattimer, J. M.; Brown, E. F. The Neutron Star Mass-Radius Relation and the Equation of State of Dense Matter. *Astrophys. J.* **2013** *765*, L5.

30. Lattimer J. M. The Nuclear Equation of State and Neutron Star Masses. *Annu. Rev. Nucl. Part. Sci.* **2012** *62*, 485.

31. Reed, B. T.; Fattoyev, F. J.; Horowitz, C. J.; Piekarewicz, J. Implications of PREX-2 on the Equation of State of Neutron-Rich Matter. *Phys. Rev. Lett.* **2021** *126*, 172503.

32. Estee, J. et al. Probing the Symmetry Energy with the Spectral Pion Ratio. *Phys. Rev. Lett.* **2021** *126*, 162701.

33. Zenihiro, J. et al. Neutron density distributions of ^{204,206,208}Pb deduced via proton elastic scattering at $E_p = 295$ MeV. *Phys. Rev. C* **2010** *82*, 044611.

34. Sotani, H.; Iida, K.; Oyamatsu, K.; Ohnishi, A. Mass and radius formulas for low-mass neutron stars. *Prog. Theor. Exp. Phys.* **2014** *2014*, 051E01.

35. Andersson, N.; Kokkotas, K. D. Gravitational Waves and Pulsating Stars: What Can We Learn from Future Observations? *Phys. Rev. Lett.* **1996** *77*, 4134.

36. Andersson, N.; Kokkotas, K. D. Towards gravitational wave asteroseismology. *Mon. Not. R. Astron. Soc.* **1998** *299*, 1059.

37. Sotani, H.; Tominaga, K.; Maeda, K. I. Density discontinuity of a neutron star and gravitational waves. *Phys. Rev. D* **2001** *65*, 024010.

38. Sotani, H.; Kohri, K.; Harada, T. Restricting quark matter models by gravitational wave observation. *Phys. Rev. D* **2004** *69*, 084008.

39. Sotani, H.; Yasutake, N.; Maruyama, T.; Tatsumi, T. Signatures of hadron-quark mixed phase in gravitational waves. *Phys. Rev. D* **2011** *83*, 024014.

40. Passamonti, A.; Andersson, N. Towards real neutron star seismology: accounting for elasticity and superfluidity. *Mon. Not. R. Astron. Soc.* **2012** *419*, 638.

41. Doneva, D. D.; Gaertig, E.; Kokkotas, K. D.; Krüger, C. Gravitational wave asteroseismology of fast rotating neutron stars with realistic equations of state. *Phys. Rev. D* **2013** *88*, 044052.

42. Krüger, C. J.; Ho, W. C. G.; Andersson, N. Seismology of adolescent neutron stars: Accounting for thermal effects and crust elasticity. *Phys. Rev. D* **2015** *92*, 063009.

43. Sotani, H. Neutron star asteroseismology and nuclear saturation parameter. *Phys. Rev. D* **2021** *103*, 123015.

44. Sotani, H.; Kumar, B. Universal relations between the quasinormal modes of neutron star and tidal deformability. *Phys. Rev. D* **2021** *104*, 123002.

45. Sotani, H.; Dohi, A. Gravitational wave asteroseismology on cooling neutron stars. *Phys. Rev. D* **2022** *105*, 023007.

46. Sotani, H.; Takiwaki, T. Gravitational wave asteroseismology with protoneutron stars. *Phys. Rev. D* **2016** *94*, 044043.

47. Sotani, H.; Kuroda, T.; Takiwaki, T.; Kotake, K. Probing mass-radius relation of protoneutron stars from gravitational-wave asteroseismology. *Phys. Rev. D* **2017** *96*, 063005.

48. Morozova, V.; Radice, D.; Burrows, A.; Vartanyan, D. The Gravitational Wave Signal from Core-collapse Supernovae. *Astrophys. J.* **2018** *861*, 10.

49. Torres-Forné, A.; Cerdá-Durán, P.; Passamonti, A.; Obergaulinger, M.; Font, J. A. Towards asteroseismology of core-collapse supernovae with gravitational wave observations – II. Inclusion of space-time perturbations. *Mon. Not. R. Astron. Soc.* **2019** *482*, 3967.

50. Sotani, H.; Sumiyoshi, K. Determination of properties of protoneutron stars toward black hole formation via gravitational wave observations. *Phys. Rev. D* **2019** *100*, 083008.

51. Sotani, H.; Takiwaki, T. Avoided crossing in gravitational wave spectra from protoneutron star. *Mon. Not. R. Astron. Soc.* **2020** *498*, 3503.

52. Sotani, H.; Takiwaki, T.; Togashi, H. Universal relation for supernova gravitational waves. *Phys. Rev. D* **2021** *104*, 123009.

53. Israel, G. L. et al. The Discovery of Rapid X-Ray Oscillations in the Tail of the SGR 1806-20 Hyperflare. *Astrophys. J.* **2005** *628*, L53.

54. Strohmayer, T. E.; Watts, A. L. Discovery of Fast X-Ray Oscillations during the 1998 Giant Flare from SGR 1900+14. *Astrophys. J.* **2005** *632*, L111.

55. Strohmayer, T. E.; Watts, A. L. The 2004 Hyperflare from SGR 1806-20: Further Evidence for Global Torsional Vibrations. *Astrophys. J.* **2006** *653*, 593.

56. Huppenkothen, D.et al. Quasi-periodic oscillations in short recurring bursts of the soft gamma repeater J1550-5418. *Astrophys. J.* **2014** *787*, 128.

57. Huppenkothen, D.; Heil, L. M.; Watts, A. L.; Göğüş, E. Quasi-Periodic Oscillations in Short Recurring Bursts of the magnetars SGR 1806-20 and SGR 1900+14 Observed With RXTE. *Astrophys. J.* **2014** *795*, 114.

58. Miller, M. C.; Chirenti, C.; Strohmayer, T. E. On the Persistence of QPOs during the SGR 1806-20 Giant Flare. *Astrophys. J.* **2019** *871*, 95.

59. Castro-Tirado, A. J. et al. Very-high-frequency oscillations in the main peak of a magnetar giant flare. *Nature* **2021** *600*, 621.

60. Sotani, H.; Kokkotas, K. D.; Stergioulas, N. Torsional oscillations of relativistic stars with dipole magnetic fields. *Mon. Not. Roy. Astron. Soc.* **2007** *375*, 261.

61. Gabler, M.; Cerdá-Durán, P.; Font, J. A.; Muller, E.; Stergioulas, N. Magneto-elastic oscillations of neutron stars II: exploring different magnetic field configurations. *Mon. Not. Roy. Astron. Soc.* **2013** *430*, 1811.

62. Gabler, M.; Cerdá-Durán, P.; Stergioulas, N. et al. Constraining properties of high-density matter in neutron stars with magneto-elastic oscillations. *Mon. Not. Roy. Astron. Soc.* **2018** *476*, 4199.

63. Steiner, A. W.; Watts, A. L. Constraints on Neutron Star Crusts from Oscillations in Giant Flares. *Phys. Rev. Lett.* **2009** *103*, 181101.

64. Gearheart, M.; Newton, W. G.; Hooker, J.; Li, B. A. Upper limits on the observational effects of nuclear pasta in neutron stars. *Mon. Not. Roy. Astron. Soc.* **2011** *418*, 2343.

65. Sotani, H.; Nakazato, K.; Iida, K.; Oyamatsu, K. Probing the Equation of State of Nuclear Matter via Neutron Star Asteroseismology. *Phys. Rev. Lett.* **2012** *108*, 201101.

66. Sotani, H.; Nakazato, K.; Iida, K.; Oyamatsu, K. Effect of superfluidity on neutron star oscillations. *Mon. Not. Roy. Astron. Soc.* **2013** *428*, L21.

67. Sotani, H.; Nakazato, K.; Iida, K.; Oyamatsu, K. Possible constraints on the density dependence of the nuclear symmetry energy from quasi-periodic oscillations in soft gamma repeaters. *Mon. Not. Roy. Astron. Soc.* **2013** *434*, 2060.

68. Deibel, A. T.; Steiner, A. W.; Brown, E. F. Magnetar giant flare oscillations and the nuclear symmetry energy. *Phys. Rev. C* **2014** *90*, 025802.

69. Sotani, H.; Iida, K.; Oyamatsu, K. Astrophysical implications of double-layer torsional oscillations in a neutron star crust as a lasagna sandwich. *Mon. Not. Roy. Astron. Soc.* **2019** *489*, 3022.

70. Troja, E.; Rosswog, S.; Gehrels, N. Precursors of short gamma-ray bursts. *Astrophys. J.* **2010** *723*, 1711.

71. Tsang, D.; Read, J. S.; Hinderer, T.; Piro, A. L.; Bondarescu, R. Resonant Shattering of Neutron Star Crusts. *Phys. Rev. Lett.* **2012** *108*, 011102.

72. Tsang, D. Shattering Flares During Close Encounters of Neutron Stars. *Astrophys. J.* **2013** *777*, 103.

73. Duncan, R. C.; Thompson, C. Formation of Very Strongly Magnetized Neutron Stars: Implications for Gamma-Ray Bursts. *Astrophys. J.* **1992** *392*, L9.

74. Thompson, C.; Duncan, R. C. The soft gamma repeaters as very strongly magnetized neutron stars - I. Radiative mechanism for outbursts. *Mon. Not. R. Astron. Soc.* **1995** *275*, 255.

75. Sotani, H.; Kokkotas, K. D.; Stergioulas, N. Neutron star mass-radius constraints using the high-frequency quasi-periodic oscillations of GRB 200415A. *Astron. Astrophys.* **2023** *676*, A65.

76. Oyamatsu, K. Nuclear shapes in the inner crust of a neutron star. *Nuclear Physics A* **1993** *561*, 431.

77. Pethick, J.; Ravenhall, D. G. Matter at Large Neutron Excess and the Physics of Neutron-Star Crusts. *Annu. Rev. Nucl. Part. Sci.* **1995** *45*, 429.

78. Oyamatsu, K.; Iida, K. Saturation of Nuclear Matter and Radii of Unstable Nuclei. *Prog. Theor. Phys.* **2003** *109*, 631.

79. Oyamatsu, K.; Iida, K. Symmetry energy at subnuclear densities and nuclei in neutron star crusts. *Phys. Rev. C* **2007** *75*, 015801.

80. Oyamatsu, K. Nuclear masses and the equation of state of nuclear matter. *Prog. Theor. Exp. Phys.* **2023** *2023*, 063D03.

81. Sotani, H.; Iida, K.; Oyamatsu, K. Probing crustal structures from neutron star compactness. *Mon. Not. R. Astron. Soc.* **2017** *470*, 4397.

82. Sotani, H. Shear and interface modes in neutron stars with pasta structures. *Phys. Rev. D* **2023** *107*, 123025.

83. Lattimer J. M. The Equation of State of Hot Dense Matter and Supernovae. *Annu. Rev. Nucl. Part. Sci.* **1981** *31*, 337.

84. Strohmayer, T.; van Horn, H. M.; Ogata, S.; Iyetomi, H.; Ichimaru, S. The Shear Modulus of the Neutron Star Crust and Nonradial Oscillations of Neutron Stars. *Astrophys. J.* **1991** *375*, 679.

85. Ogata, S.; Ichimaru, S. First-principles calculations of shear moduli for Monte Carlo–simulated Coulomb solids. *Phys. Rev. A* **1990** *42*, 4867.

86. Baiko, D. A. Shear modulus of neutron star crust. *Mon. Not. R. Astron. Soc.* **2011** *416*, 22.

87. Kobyakov, D.; Pethick, C. J. Dynamics of the inner crust of neutron stars: Hydrodynamics, elasticity, and collective modes. *Phys. Rev. C* **2013** *87*, 055803.

88. Sotani H. Electron screening effects on crustal torsional oscillations. *Phys. Lett. B* **2014** *730*, 166.

89. Kobyakov, D.; Pethick, C. J. Elastic properties of polycrystalline dense matter. *Mon. Not. R. Astron. Soc.* **2015** *449*, L110.

90. Sotani, H.; Togashi, H.; Takano, M. Effects of finite sizes of atomic nuclei on shear modulus and torsional oscillations in neutron stars. *Mon. Not. R. Astron. Soc.* **2022** *516*, 5440.

91. Pethick, C. J.; Potekhin, A. Y. Liquid crystals in the mantles of neutron stars. *Phys. Lett. B* **1998** *427*, 7.

92. Caplan, M. E.; Schneider, A. S.; Horowitz, C. J. Elasticity of Nuclear Pasta. *Phys. Rev. Lett.* **2018** *121*, 132701.

93. Pethick, C. J.; Zhang, Z.-W.; Kobyakov, D. N. Elastic properties of phases with nonspherical nuclei in dense matter. *Phys. Rev. C* **2020** *101*, 055802.

94. Sotani, H.; Iida, K.; Oyamatsu, K. Probing nuclear bubble structure via neutron star asteroseismology. *Mon. Not. Roy. Astron. Soc.* **2017** *470*, 4397.

95. Schumaker, B. L.; Thorne, K. S. Torsional oscillations of neutron stars. *Mon. Not. Roy. Astron. Soc.* **1983** *203*, 457.

96. Sotani, H.; Iida, K.; Oyamatsu, K. Constraints on the nuclear equation of state and the neutron star structure from crustal torsional oscillations. *Mon. Not. Roy. Astron. Soc.* **2018** *479*, 4735.

97. Chamel, N. Neutron conduction in the inner crust of a neutron star in the framework of the band theory of solids. *Phys. Rev. C* **2012** *85*, 035801.

98. Chamel, N. Band structure effects for dripped neutrons in neutron star crust. *Nucl. Phys. A* **2005** *747*, 109.

99. Carter, B.; Chamel, N.; Haensel, P. Entrainment coefficient and effective mass for conduction neutrons in neutron star crust: simple microscopic models. *Nucl. Phys. A* **2005** *748*, 675.

100. Watanabe, G.; Pethick, C. J. Superfluid Density of Neutrons in the Inner Crust of Neutron Stars: New Life for Pulsar Glitch Models. *Phys. Rev. Lett.* **2017** *119*, 062701.
101. Hansen, C. J.; Cioffi, D. F. Torsional oscillations in neutron star crusts. *Astrophys. J.* **1980** *238*, 740.
102. Sotani, H. Constraints on Pasta Structure of Neutron Stars from Oscillations in Giant Flares. *Mon. Not. Roy. Astron. Soc.* **2011** *417*, L70.
103. Sotani, H.; Iida, K.; Oyamatsu, K. Possible identifications of newly observed magnetar quasi-periodic oscillations as crustal shear modes. *New Astron.* **2016** *43*, 80.
104. Sotani, H. Empirical formula of crustal torsional oscillations. *Phys. Rev. D* **2016** *93*, 044059.
105. Bauswein, A.; Just, O.; Janka, H.-T.; Stergioulas, N. Neutron-star Radius Constraints from GW170817 and Future Detections. *Astrophys. J.* **2017** *850*, L34.
106. Capano, C. D. et al. Stringent constraints on neutron-star radii from multimessenger observations and nuclear theory. *Nat. Astron.* **2020** *4*, 625.
107. Dietrich, T. et al. Multimessenger constraints on the neutron-star equation of state and the Hubble constant. *Science* **2020** *370*, 1450.
108. Romani, R. W. et. al. PSR J0952-0607: The Fastest and Heaviest Known Galactic Neutron Star. *Astrophys. J.* **2022** *934*, L17.
109. Yoshida, S; Lee, U. Nonradial oscillations of neutron stars with a solid crust. *Astron. Astrophys.* **2002** *395*, 201.
110. Finn, L. S. Non-radial pulsations of neutron stars with a crust. *Mon. Not. Roy. Astron. Soc.* **1990** *245*, 82.
111. Gudmundsson, E. H.; Pethick, C. J.; Epstein, R. I. Structure of neutron star envelopes. *Astrophys. J.* **1983** *272*, 286.
112. Sotani H. Shear oscillations in neutron stars and the nuclear symmetry energy. *Phys. Rev. D* **2024** *109*, 023030.
113. Piro, A. L.; Bildsten, L. Neutron Star Crustal Interface Waves. *Astrophys. J.* **2005** *619*, 1054.
114. Sotani H. Effect of nuclear saturation parameters on a possible maximum mass of neutron stars. *Phys. Rev. C* **2017** *95*, 025802.
115. Maruyama, T.; Chiba, S.; Schulze, H.-J.; Tatsumi, T. Hadron-quark mixed phase in hyperon stars. *Phys. Rev. D* **2007** *76*, 123015.
116. Xia, C.-J.; Maruyama, T., Yasutake, N.; Tatsumi, T.; Shen, H.; Togashi, H. Systematic study on the quark-hadron mixed phase in compact stars. *Phys. Rev. D* **2020** *102*, 023031.
117. Sotani, H.; Maruyama, T.; Tatsum, T. Shear oscillations in the hadron-quark mixed phase. *Nucl. Phys. A* **2013** 906, 37.
118. Lau, S. Y.; Yagi, K. Probing hybrid stars with gravitational waves via interfacial modes. *Phys. Rev. D* **2021** *103*, 063015.